Scholars' Mine

Masters Theses   Student Theses and Dissertations

Spring 2005

Application of laser aided manufacturing process for functionally graded thermal barrier coatings

Yashodhan Joshi

Follow this and additional works at: https://scholarsmine.mst.edu/masters_theses

Part of the Manufacturing Commons

Department:

APPLICATION OF LASER AIDED MANUFACTURING PROCESS FOR FUNCTIONALLY GRADED THERMAL BARRIER COATINGS

by

YASHODHAN JOSHI

A THESIS

Presented to the Faculty of the Graduate School of the

UNIVERSITY OF MISSOURI-ROLLA

In Partial Fulfillment of the Requirements for the Degree

MASTER OF SCIENCE IN MANUFACTURING ENGINEERING

2005

Approved by

_____   _____
F.W. Liou, Advisor   R.G. Landers

_____
K. Chandrashekhara

ABSTRACT

Laser Aided Manufacturing Process (LAMP) is a rapid prototyping process used to build three dimensional functional metal and ceramic parts. The process developed in the LAMP laboratory at University of Missouri-Rolla uses a 5-axis fadal CNC machine and a 2.5 KW Nd:YAG (TEM$_{00}$) Rofin Sinar laser. The laser power and metal/ceramic powder are the input along with auxiliary systems such as shielding gas delivery, RT data acquisition, coolant system. The hybrid process makes use of metal deposition and machining to obtain parts meeting design tolerances.

LAMP is used to improve upon the process of Thermal Barrier Coating (TBC) deposition and enhance the material properties of TBC. LAMP is proposed to give better bond strength as a metallurgical bond is formed between the coating and the substrate. Improved life and operating temperatures of the coatings can result in increased efficiency of operation of the turbines and engines and result in better cost efficiency. Functional grading of the 8% Yittria stabilized Zirconia and NiCoCrAlY TBC is evaluated for thermo mechanical properties such as surface roughness, porosity to evaluate the deposition quality. The LAMP is optimized by using Taguchi method of Design of Experiments to obtain the improved TBC. The variation of the influence of various control factors with the changing composition of NiCoCrAlY and Zirconia is studied and influential control factors are identified. The variation of energy density as a function of surface roughness and material composition is plotted. The coating is characterized by residual stress, microhardness and microstructure analysis.

ACKNOWLEDGMENTS

I express my sincere thanks to my advisor Dr. Frank Liou who kept faith in me and gave me invaluable moral and financial support and guided me through my research work with his suggestions.

I thank my committee members Dr. Robert Landers and Dr. K. Chandrashekhara for taking interest in my research. Also there are numerous helping hands that have helped me in my work. I would like to thank Dr. Newkirk, Dr. Peaslee, Dr. Van Aken, Mr. Eric Bohemian and Dr. Scott Miller for their help and suggestions in the metallurgical aspects of my research. My colleagues have helped me time and again in my research. Mr. Bob Hribar and Mr. Mitch Cottrell need a special mention for their help.

Thanks to my friends for their moral encouragement and help throughout my stay and work at UMR. I thank my parents to whom I owe my existence and wellbeing and my brother for his support. A final thanks to the almighty who has been my constant source of inspiration during the difficult times.

TABLE OF CONTENTS

LIST OF ILLUSTRATIONS

LIST OF TABLES

NOMENCLATURE

Symbol	Description
σ_t	Thermal Stress
υ	Poisson's Ratio
λ	Wavelength
θ	Diffraction Angle
ψ	Angle of Tilt
φ	Angle made by resultant surface stress with the principal stress
$\sigma 1$	Principal stress1
$\sigma 2$	Principal stress2
$\sigma 3$	Principal stress perpendicular to the surface
$\varepsilon_{\psi\varphi}$	Strain along a direction defined by ψ and φ
HV	Vickers hardness value

1. INTRODUCTION

1.1. TURBINE ENGINES

The turbine engines operate at high inlet gas temperatures of around 1200^0 C. The power and efficiency of the turbines are very sensitive to the operating temperatures. There has been a constant endeavor to increase the operating temperatures for this reason.

Material development for turbine blades and vanes found in the hot section of turbine blades is very important and has led to material advancements like directional grain growth and single crystal alloy development. This material has to endure extremely hot engine gases, corrosive and oxidative environment, large centrifugal loads and high velocity foreign object impacts. This makes them necessary to have high temperature strength, toughness and corrosion and oxidation resistance. This has lead to the development of Nickel based super alloys used as the material of choice for these applications.

Internal cooling of turbine blades by coolant air is used to enhance the high temperature operating ability but it reduces the efficiency as the air gets mixed with the hot inlet gases and reduces the gas temperature.

Thermal Barrier Coatings are the solution to the problem of operating the engines at increasingly higher temperatures. Thermal barrier Coatings consist of a metal bond coat which forms a protective alumina oxide layer and a thermally insulating ceramic top coat which is generally of yittria stabilized zirconia. These coatings provide thermal and oxidation resistance and produce a temperature drop across them enabling the usage of conventional super alloys at high temperatures. Temperature drops of 170^0C have been reported across 150 μ m thick coatings [15].

1.2. STUDY OBJECTIVE

This thesis studies the promising technology of Laser Aided Manufacturing Process (LAMP) as a means of applying TBC. Functional grading of the TBC is carried for gradual variation of the material properties which enables design of TBC at required location. The process parameters are studied to obtain optimum values for good depositions measured by the surface roughness of the depositions. The relative influence

of the process parameters is studied for the functionally graded TBC. Design of Experiments (DOE) by Taguchi Analysis is used.

1.3. ADVANTAGES OF LAMP

Advantages of LAMP process for the Thermal Barrier Coatings are as follows:

1. The localized repair of the coatings is possible with cost and time advantages.

2. The LAMP process gives a localized source of energy where the size of laser beam can be controlled with precision and forms a perfect metallurgical bond between the clad layer and the substrate by superficial melting of the substrate.

3. LAMP process gives a better control of the compositional variation of the material in the FGM.

4. Excellent coating properties obtained due to fine grain size of laser deposited materials.

5. Low dilution.

6. Minimum changes in base material due to low heat load.

7. Controllable coating thickness.

8. Reasonable productivity and cost make laser coating attractive for industrial coating of new components and in repair.

9. Rapid heating and cooling of the deposited material cause fine grain structure which reduces crack propagation, thus increasing the life of the coating.

Table 1.1 compares the properties of deposition obtained by thermal spraying, weld surfacing and laser deposition.

Table 1.1. Comparison of thermal spraying, weld surfacing and laser coating

Coating process	Thermal spraying	Weld surfacing	Laser coating
Heat source	Combustion flame, electric plasma arc	Combustion flame, electric arc	High intensity laser radiation
Bond strength	Low to moderate mechanical bonding	High metallurgical bonding	High metallurgical bonding
Coating structure	Lamellar; from porous to nearly dense	Dense; cracks and pores may exist	Dense; crack and pore-free layers
Heat load to workpiece	Very low to moderate	Very high	Low to moderate
Dilution	Nil	Moderate to high	Low
Coating thickness	0.05 – some mm's	Several mm	Typically 0.5 – 3 mm
Coating materials	Wide range of metals, alloys, hard metal, ceramics, polymers	Metal and alloys; alloys with hard particles	Metal and alloys; alloys with hard particles; hard metals, ceramics

Table 1.1. Comparison of thermal spraying, weld surfacing and laser coating (cont)

Productivity	Low to high	Low to very high	Low to moderate/ (high)
Cost	Low to high	Low to moderate	Moderate to high

2. THERMAL BARRIER COATING

2.1. OVERVIEW AND COMPOSITION

The TBC is required to limit thermal heat transfer across it and protect the engine components from oxidation and corrosion. No single material satisfies all the objectives. The TBC is conventionally composed of three layers. The outer ceramic layer limits heat transfer across it while the inner metal bond coat adheres to the substrate and remains relatively stress free and forms a thermally grown oxide layer which provides adhering surface for the ceramic layer. The ceramic layer is likely to have a thermal expansion coefficient that differs from the component to which it is applied. This layer should therefore have a high in-plane compliance to accommodate the thermal expansion mismatch between the TBC and the underlying nickel super alloy component. In addition, it must be able to retain this property and its low thermal conductivity during prolonged environmental exposure.

The ceramic layers have a tendency to spall upon experiencing thermal cycling from ambient conditions to high operating temperatures. Certain compositions of TBC have been found to extend the coating life and life prediction models have been formulated to permit the utilization of thermal barriers in a way that maximizes the benefits. It has been discovered through cyclic testing that yittria stabilized zirconia (YSZ) with 6-8 wt. % significantly lengthens the spallation life of the ceramic at temperatures above 982 [2, 8]. YSZ also has a coefficient of thermal expansion (CTE) which better matches the Ni super alloy substrate. This match results in a residual stress reduction, which also prolongs the life of the component. Table 2.1. compares the properties of different ceramic materials used in TBC.

An inner metallic or sometimes alluminide intermetallic bond coat rich in Al is used to anchor the TBC to the nickel superalloy coating. This coat performs two functions:

1) The Al provides oxides to form an oxidation resistant layer that protects the superalloy substrate and

2) The bond coat strongly adheres to the ceramic layer and chemically to the underlying Ni based super alloy substrate structure.

Because the pores in LPPS coatings are transverse to the heat flow direction, these coatings have an even lower thermal conductivity than the ceramic they are synthesized from.

The ceramic grows into an individual, free-standing columnar structure with intercolumnar pores. These columns are each tightly bound to the oxide film on the bond coat. But because they are more or less individual columns, they are essentially free to separate from adjacent columns upon lateral thermal expansion. The crystal orientation is also highly textured along which have a low transverse modulus. Consequently, this structure prevents the build-up of long range stresses and yields good thermal shock resistance. In addition, the columnar pores positioned between the YSZ columns will decrease the dielectric constant of the ceramic. As seen in Figure 2.1, the cross-section of a TBC is shown.

Table 2.1. Comparison of ceramic properties used in TBC [3]

Mechanical & Thermal Properties	Units	(Coors AD-99.5) Al_2O_3	MSZ (3 wt.% MgO)	YSZ (~ 8 wt.%) Y_2O_3	YSZ (>12 wt.%) Y_2O_3
Density	g/cm3	3.89	5.75	6.02	5.6
Elastic Mod.	GPa	372	200	200	173
Compressive Strength	MPa	2620	1750		

Table 2.1. Comparison of ceramic properties used in TBC [3] (cont)

Thermal Conductivity	W/m-°K	35.6	2.2	2.2	2.2
CTE	$10 6 - °C/$	8.2	10.1	10.3	10.5
Specific Heat	J/kg-°K	880	486		
Thermal Shock Resistance	□C	200	350	350	150
Max. Use Temp.	□C	1750	500	2400	2400

2.2. TBC MATERIAL AND PROCESS SELECTION MODEL

The selection of the materials and the appropriate process for the TBC deposition is very important. The process and material properties have impact on the TBC properties. As seen in Figure 2.2, the various important coating material and process properties are shown.

2.3. FUNCTIONALLY GRADED THERMAL BARRIER COATINGS

The functionally graded materials (FGM) are developed for the purpose of use as a protective coating for the metallic elements, which are subjected to thermal loads due to high temperature environment (up to a temperature of 2000 °K), cyclical changes of temperature.
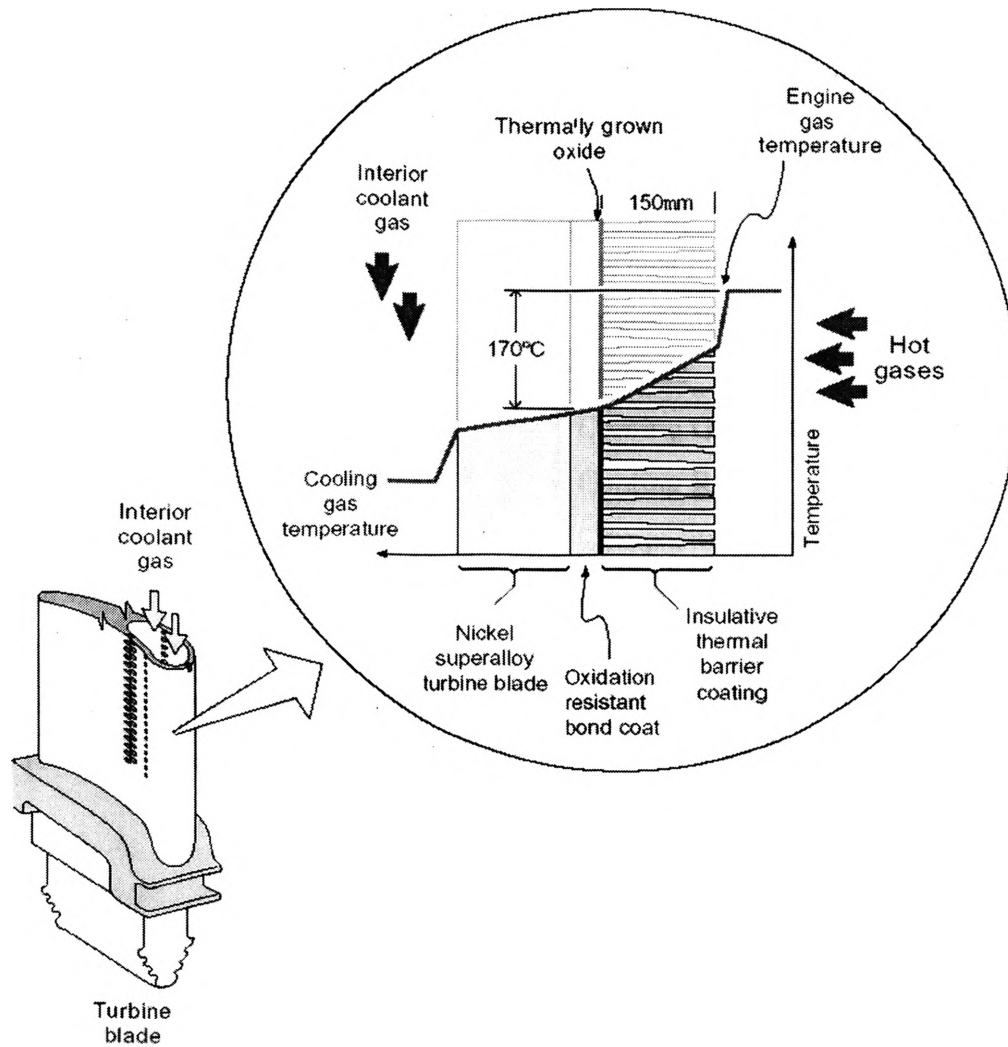
Figure 2.1. TBC cross section [6]

Increase in the bond strength and the reduction in the residual stresses and 5 times better thermal cycle resistance of FGM coatings over duplex coatings has been reported in a study on plasma sprayed functionally graded TBC.[1].

[10] Elperin and Rudin talk about the equation:

$$V_m = V_0 + \left(\frac{z}{\Delta}\right)^k (V_1 - V_0), \; k > 0$$

(1)

```
                        ┌──────────────┐
                        │     TBC      │
                        └──────────────┘
        ┌────────────────────────┐  ┌────────────────────────┐
        │ Coating Material        │  │ Coating Process         │
        │ Properties              │  │ Properties              │
        └────────────────────────┘  └────────────────────────┘
```

Coating Material Properties	Coating Process Properties
Hardness/Toughness	Surface preparation
Chemical Stability	Temperature
Substrate Compatibility	Pressure
Density	Coating Geometry
Thermal Expansion	Coating Rate
Thermal Conductivity	Composition Control
Electrical Resistance	Uniformity
Melting Temperature	Porosity
Modulus of Elasticity	Surface Finish
Phase Transformations	Multilayer Capability
	Graded layer capability
	Batch/Continuous
	Scale
	Economy

Figure 2.2. TBC material and process selection model [3]

used to determine the dependence of temperature and thermal stresses distribution on the parameters such as V1, V0 and k. Calculations showed that the thermal stresses, in contrast to the temperature, strongly depend on the profile of $V_m(z)$ in a coating. It is possible to decrease by several times the thermal stresses in a coating changing an exponent k (provided that V_c is fixed). This allows us to minimize the thermal stresses and to improve the thermal reliability of a coating.

For example, if the coating material has a very different thermal-expansion coefficient than the substrate, there is the possibility of severe stresses building at the

interface and resulting in a crack. A common way to circumvent this problem is to optimize the coating thickness or to introduce a compliant interlayer for the reduction of the thermal stress. Unfortunately, most compliant films also melt at lower temperature. A recent development by Jasim et al.[11] is a functionally graded coating (FGC) built up by three overlaid laser tracks in which the proportion of SiC reinforcement increased in steps from 10 vol.% to 50 vol.%. Their work showed the possibility of laser processing to deposit a thick multilayer of essentially discrete composition rather than a gradual composition change.

2.4. MECHANISMS CONTROLLING LIFETIMES OF TBCS

The various mechanisms limiting the life of thermal barrier coatings are

2.4.1. Chemical Reactions. The chemical reactions that affect the TBC are

1. Interdiffusion substrate-bond coat-ceramic

2. Oxidation of bond coat

3. Oxygen diffusion through zirconia

4. Corrosive attack on zirconia surface

2.4.2. Structural Changes. The structural changes affecting the TBCs are

1. Formation of new phases at interface substrate-bond coat

2. Formation of new phases at interface bond coat-zirconia

3. Phase changes in the zirconia

4. Grain growth in the zirconia or sintering

2.4.3. Mechanical Degradation. The mechanical degradation effects on TBC are

1. Spallation at interfaces or inside the zirconia

2. Crack growth perpendicular or parallel to the coated surface

3. Thermal fatigue, thermal shock

4. Creep

5. Reduction of fracture toughness

6. Change of weibull modulus

7. Change of strength and hardness

8. Change of ductility

9. Change of elastic modulus

10. Change of density

11. Erosion.

2.4.4. Surface Roughness of the Bond Coating. For EB-PVD the surface smoothness influences the microstructure with increasing surface roughness the width lamellae increases as well as the deviation from ideal microstructure [11]. Ahmaniemi et.al discuss about the coating microstructures that can be controlled by spray parameters, including temperature control of the substrate and the coating during the deposition. If the system heats up too much in spraying, compressive stresses will be developed into the coating structure. For that reason active substrate and surface cooling are normally used during spraying. Spray parameters can also be fixed to obtain desired level of porosity and micro cracks. Vertical segmentation cracks, which go through the whole coating, can be produced by introducing rather thick spray passes [9]. In addition to strain tolerance, pores and especially the horizontal cracks are naturally advantageous in lowering the thermal conductivity of the coating.

2.4.5. Effect of Microstructure on Residual Stresses in TBC. Crystals nucleate randomly on the substrate and grow until they impinge and form grain boundaries between them. In this impingement process, free surfaces are converted into grain boundaries. Energetically, this allows the difference between the surface and grain boundary energies to be converted into strain energy, resulting into a tensile stress in the continuous film. Any densification process in a formed film, such as the annihilation of vacancies at free surfaces or grain boundaries and the elimination of grain boundaries by grain growth, causes tensile stresses as well.

2.4.6. Substrate Temperature. This affects surface diffusion of deposited zirconium, yttrium and oxygen, as well as nucleation of stable oxide particles and their growth rate. Surface diffusion and growth rate of oxide particles have a major influence on the TBC microstructure. [1]

2.4.7. Effect of Porosity on Young's Modulus. The increase in porosity decreases the young's modulus as shown by the weibull plot of young's modulus in [1]. The relation between the thermal stress and the elastic modulus is gives by (8)

$$\sigma_t = \frac{E \Delta \alpha \Delta T}{1 - \vartheta^2}$$

(2)

where E is the elastic modulus, ϑ is the Poisson's ratio and ΔT is the temperature difference between the soak temperature and the ambient. This explains, as the elastic modulus decreases the thermal stresses are reduced.

2.4.8. Effect of Mechanical Properties of Bond Coat on the Residual Stress in Coatings. Young's modulus and CTE affect the thermal expansion mismatch stresses between the bond coat and the TBC. With an increasing CTE of the bond coat mismatch stresses will also increase. The CTE of NiCoCrAlY was found to be greater than that of super alloy in the operating range of temperature, so that such a bond coating would experience transient compressive creep on heating to temperature according to I.G.Wright and B.A. Pint [6].

The alluminide intermetallic phase coatings are brittle at low temperatures and ductile at high temperatures. This temperature is called ductile to brittle transition temperature (DBTT) at which this change takes place.

It is important that this DBTT is as low as possible so that this transition does not occur in service since the cracks may then propagate into the substrate. NiCoCrAlY coatings containing 20 to 26 % cobalt are significantly more ductile than either NiCrAlY or CoCrAlY coatings according to Bernstein et al. [4].

2.4.9. Effect of Microstructure of Top Coat on the TBC Failure. The crack initiation and propagation behavior under tensile loading depends strongly on the micro-structure of TBC systems. For TBC systems with large numbers of micro cracks in the top-coat, the macro crack development is appreciably delayed, mainly by virtue of the effective stress relief associated with the opening of the individual micro cracks as compared with the TBC systems with only a few micro cracks.

The compressive failure of TBC systems is rather incidental and depends strongly on the strength of top-coat at the interfacial region which is affected by the presence of the micro cracks and pores. [2]

2.4.10. Stress Strain Behavior of TBCs. A literature review shows that typical fracture stresses are in the range from 500 to 700 Mpa; the corresponding fracture strains under tensile conditions lie between 0.1 to 0.4 %.Strain of 0.1 to 0.2% results in the initiation of cracks at the TBC surface; these then grow perpendicular to the surface through the ceramic coating, if strain is further increased. Close to the bond coat/TBC interface, cracks become deflected and further crack growth occurs parallel to the bond coat/TBC interface. Cracks always initiate at surface pores of the TBC. Further increase of strain results in crack growth and linking up of cracks to form a crack network. The critical strains required for TBC spallation of EB-PVD coatings seem to be slightly higher compared with APS coatings due to the fine-grained lamellar microstructure of the former and their lower values of Young's modulus.

2.4.11. Corrosion. Three types of corrosions have been identified. A layer type corrosion identified by an uneven base-metal oxide interface and the absence of subscale sulfides known as Type II corrosion occurs below about 700 EC. A non layer type corrosion (type I) identified by a smooth base metal-oxide interface and a uniform depleted zone containing discrete sulfide particles beneath the oxide scale has been found to occur above 775EC.

Above 1700EF oxidation takes over as the primary corrosion mechanism.

3. DOE BY TAGUCHI ANALYSIS

3.1. TAGUCHI THEORY

The Taguchi Design of Experiments was implemented for optimization of the LAMP parameters to improve the quality for the selected Quality Characteristics.

Improving quality consisted of reducing the distance of the population mean to the target and by reducing the standard deviation of the population performance.

The approach to obtain the objective consists of the following:

1. Planning
2. Designing
3. Conducting
4. Analyzing
5. Confirming

3.2. PLANNING

The planning of experiments consists of deciding on the factors, quality characteristics and the results.

3.2.1. Factors. The various variables that seem to influence the intended objectives are called factors. Only those factors that are considered to have a direct influence on the output and those that are included in the investigation are considered as factors in the DOE study.

The levels of each factor are decided. Selecting two levels of factors assumes to have a linear relationship between the factor and the result.

3.2.2. Result. A result is a measure of performance. The results are quantified even when they are qualitative on a scale of 1 to 10. In a case where multiple evaluations are combined in a single index an Overall Evaluation Criterion (OEC) is formed.

Quality Characteristic- The results are compared on three turfs as follows:

Bigger is better

Smaller is better

Nominal is best

3.2.3. Design of Experiments. Orthogonal arrays are used to design experiments. On the basis of the number of factors and their levels orthogonal arrays to fit in the factors are chosen.

3.3. ANALYSIS

The analysis of results is carried out to check the objective of reducing the gap between the mean and predicted mean and reduced variance.

3.3.1. Simple Analysis. It is carried out to produce a grand average of results and the average effects of factors.

1. Factor influence or main effects

2. Optimum condition for a desired quality characteristic

3. Performance expected at the optimum condition.

3.3.2. Analysis of Variance. It is carried out to give

1. Relative influence of factor and interaction to the variation of results.

2. Test of significance of factor and interactions assigned to the column.

3. Confidence interval (C.I) on optimum performance

4. Confidence interval on main effect of factors.

5. Error factor/term which includes effect of factors which have not been included and experimental error.

3.3.3. Analysis Formulae. The average effect of a factor at a level is calculated. The average effects of all the factors are calculated for all the results obtained for each factor level is given by

$$\overline{A_1} = \frac{Y_1 + Y_2}{2} \tag{3}$$

where $\overline{A_1}$ is the average effect with factor A at first level with Y_1 and Y_2 as the experiment results with factor A at first level. When average factor level effect is plotted against the factor levels, the plot shows the nature of trend of influence of the factor to the result and it indicates variation in results for the shift in factor levels proportional to the slope of the difference between the endpoints.

Result expected at optimum condition is an estimate of performance at the optimum condition. The performance expected is calculated by adding all improvements from all factors to the grand average of performance.

The main objective of ANOVA is to extract from the results how much variation each factor or interaction causes relative to the total variation observed in the result. The total and factor sum of squares are the basic calculations needed for ANOVA. Total sum of squares is calculated as,

$$S_T = \sum_{i=1}^{N} Y_i^2 - \frac{T^2}{N} \tag{4}$$

Factor sum of squares is given as,

$$S_A = \frac{A_1^2}{N_{A1}} + \frac{A_2^2}{N_{A2}} - C.F. \tag{5}$$

Where C.F. is correction factor $= \dfrac{T^2}{N}$ (6)

Mean squares (variance): $V_A = \dfrac{S_A}{f_A}$ (7)

F-ratio: $F_A = \dfrac{V_A}{V_e}$ (8)

Pure sum of squares: $S_A' = S_A - (V_e * f_A)$ (9)

Percent influence: $P_A = \dfrac{S_A'}{S_T}$ (10)

The confidence interval (C.I) represents the boundaries on the expected results and is always calculated at a confidence level.

$$\text{Confidence Interval (C.I)} = \pm \left[\frac{F(1, n_2) * V_e}{N_e} \right]^{0.5} \tag{11}$$

Where F is the F value from the F table for the factor DOF and the error DOF at the confidence interval desired, V_e is the variance of the error term and N_e is the effective number of replications.

4. PROBLEM, MATERIAL SELECTION AND EXPERIMENTAL SETTINGS

4.1. PROBLEM

LAMP is used to improve upon the process of TBC deposition and enhance the material properties of TBCs and improve the life of the coatings. Improved life and operating temperatures of the coatings can result in increased efficiency of operation of the turbines and engines and result in better cost efficiency.

LAMP is proposed to give better bond strength as a metallurgical bond is formed between the coating and the substrate.

The FGM reduces the residual stresses accumulated in the TBCs due to gradual variation of properties between the bond coat and the zirconium top coat along with the material composition variation.

The effect of LAMP process parameters on the TBC properties is studied and the optimization of LAMP parameters is carried out to obtain the TBC deposition with following desired characteristics

Reduced residual stress

Improved adhesion between the TBC and the substrate

Better life time of coatings

Porosity

Hardness

Effect of microstructure on the TBC properties

Surface roughness

The factors considered for the DOE were

1. Power density

2. Outer gas

3. Inner gas

4. Layer thickness

5. Powder flow rate

6. Powder size

7. Overlap

4.2. MATERIAL SELECTION

The material selection was done for three different materials.

The TBC consists of three parts which differ in material and which together form the TBC.

4.2.1. 316L Stainless Steel as the Substrate Material. The modern turbine blades are made of single crystal Nickel based super alloys. These super alloys being costly an alternative was searched for it which would have properties similar to it at room temperature. As the study pertained to the evaluation and optimization of properties of LAMP FGM TBC depositions high temperature behavior of the materials was not taken into consideration.

The various alternatives that were taken into account are

Rene'5

Rene'41

316L stainless steel

SUS340m stainless steel

The selection criteria for the material selection were-

The material should have similar mechanical and thermal properties similar to that of super alloys at room temperature.

The material should be cheaply available.

The material should be easily available.

The material should have good thermal conductivity.

316L stainless steel fits all these requirements and was chosen as the substrate material.

Some properties of stainless steel are-

Tensile strength ultimate – 520-670 MPa

Tensile strength yield- 310 MPa

Modulus of Elasticity- 200 GPa

CTE linear, 100^0 C- 16.5 $\mu m / m - °C$

4.2.2. NiCoCrAlY as Bond Coat. Mechanical and thermal properties of NiCoCrAlY are as follows:

Density 5% of theoretical – 0.42g/cc

Melting temperature- 1315 ^{0}C

CTE (20 to 200)-17 $\mu in/in°C$

Thermal Conductivity- 0.03 Cal/cm^2 ^{0}C

The potential candidates for the bond coat were –

NiCoCrAlY

Alluminide bond coats

NiCoCrAlY was chosen over the Ni-Al bond coat because of the close match between it's CTE and that of the substrate. Powder was obtained from Praxair.

4.2.3. Yittria Stabilized Zirconia as the Ceramic Material. Yittria stabilized zirconia has the following properties

Melting Temperature- 2700 C

CTE - 6.5 x 10^{-6} to 10.5 x 10^{-6} /C

Thermal Conductivity – 8 Btu/ft^2/in/F.

Addition of more than 16 mol % MgO (5.86 wt %), or 8 mol% of Y2O3 (13.75 wt %), into zirconia structure is needed to form a fully stabilized zirconia. Its structure becomes cubic solid solution, which has no phase transformation up to 2,500 C.

4.3. EXPERIMENTAL SETTINGS

The different factors and the various levels of each factor are given below

1. Overlap- 0.25, 0.45

2. Feedrate- 20, 40 IPM

3. Power-   500, 700 W

4. Outer gas- 10, 12. PSI

5. Inner gas- 4, 6. PSI

6. Powder flow rate- The powder flow rate of the two screw powder feeders was varied from 0 to 1 volt so that the resultant weight ratio of the two powders NiCoCrAlY/zirconia in the depositions will vary from 100/0 to 0/100 in 6 discreet steps. The variation in the powder flow for both the powder feeders is not linear and hence the variation in the voltage is not in equidistant steps.

The calibrated values of the two powder feeders for the corresponding voltages are given in Table 4.1.

7. Standoff distance- 0.25, 0.35 inches

Table 4.1. Powder flow voltage variation in the FGM deposition

	NiCoCrAlY Powder Feeder voltage	NiCoCrAlY Powder Feeder mass flow rate	Zirconia Powder Feeder voltage	Zirconia Powder Feeder mass flow rate
100/0	1	0.85g/min	0g/min	0g/min
80/20	1	0.85g/min	0.6	0.24g/min
60/40	1	0.85g/min	0.7	0.5g/min
40/60	0.7	0.4g/min	1	0.58g/min
20/80	0.6	0.14g/min	1	0.58g/min
0/100	0	0g/min	1	0.58g/min

4.4. ORTHOGONAL ARRAY SELECTION

The resultant depositions were evaluated for surface roughness, which was measured in inches. The Qualitek software was used for the statistical Taguchi Analysis of the data. Two Quality characteristics were taken into account. The surface roughness was considered as smaller is better. The samples were also rated by visual inspection from 1 to 10 with smaller is better quality characteristic. An Overall Evaluation Criterion (OEC) was formed and standard analysis was performed on the data. The Main Effects, ANOVA Effects and Optimum Performance were studied for each layer of FGM. This study was repeated six times for each layer of FGM, which would henceforth be called percentage setting in this article, starting from 100% NiCoCrAlY: 0% Zirconia, 80% NiCoCrAlY: 20% Zirconia, 60% NiCoCrAlY: 40% Zirconia, 40% NiCoCrAlY: 60% Zirconia, 20% NiCoCrAlY: 80% Zirconia and 0% NiCoCrAlY: 100% Zirconia.

L-12 orthogonal array was selected for Taguchi Analysis. The results are analyzed for the following:

The optimum design

Influence of individual factors

Relative influence of individual factors

Plot graphs of factor influence, main effects, contribution.

An L-12 array was chosen and a replica of each setting was deposited. The total number of experiments run is 144. As seen in Figure 4.1, the inner array design window of the Qualitek software, where the values for the control factors are entered is shown.

Inner Array Design

Array Type: **L-12**

Use <ctrl> + <arrows> to move cursor.

Print | Ok
Help | Cancel

	Factors	Level 1	Level 2	Level 3	Level 4
1	Inter	*UNUSED*	-----------	-----------	-----------
2	Inter	*UNUSED*	-----------	-----------	-----------
3	Overlap	25	45	-----------	-----------
4	Feedrate	20	40	-----------	-----------
5	COLUMN UNUSED	*UNUSED*	-----------	-----------	-----------
6	Power	500	700	-----------	-----------
7	Inter	*UNUSED*	-----------	-----------	-----------
8	Outer gas	8	12	-----------	-----------
9	Powder flow rate	lower	higher	-----------	-----------
10	Inner gas	4	6	-----------	-----------
11	Standoff distance	25	35	-----------	-----------

Col Inter | Inter Table | Reset Col | Delete Cell | Unused | Upgrade | Test

Figure 4.1. Inner array design

Each row has been allotted for a different setting of experiment in the L-12 array. The factors not included in the study have empty columns and are denoted by 0. As seen in Figure 4.2, the inner array designed for the experiments which is L-12 orthogonal array is shown. There are total 12 settings of experiments. 1 represents the first level of the control factor while 2 is the higher level of the control factor.

Edit Inner Array — ☐ ✕

Array Type: **L - 12**

Ok
Cancel
Help
Print
Examine

	1	2	3	4	5	6	7	8	9	10	11
1	0	0	1	1	0	1	0	1	1	1	1
2	0	0	1	1	0	2	0	2	2	2	2
3	0	0	2	2	0	1	0	1	2	2	2
4	0	0	1	2	0	1	0	2	1	1	2
5	0	0	2	1	0	2	0	2	1	2	1
6	0	0	2	2	0	2	0	1	2	1	1
7	0	0	2	2	0	1	0	2	1	2	1
8	0	0	2	1	0	2	0	1	1	1	2
9	0	0	1	2	0	2	0	2	2	1	1
10	0	0	2	1	0	1	0	2	2	1	2
11	0	0	1	2	0	2	0	1	1	2	2
12	0	0	1	1	0	1	0	1	2	2	1
Total	0	0	18	18	0	18	0	18	18	18	18

Reset Col   Reset Array

Figure 4.2. Inner Array

5. RESULTS

5.1. 100% NICOCRAIY AND 0 % ZIRCONIA

The deposition consisted of 1 layer of 100% NiCoCrAlY. As seen in Figure 5.1, a smooth shiny deposition for 100% NiCoCrAlY layer is obtained on the substrate which is devoid of cracks and pores.
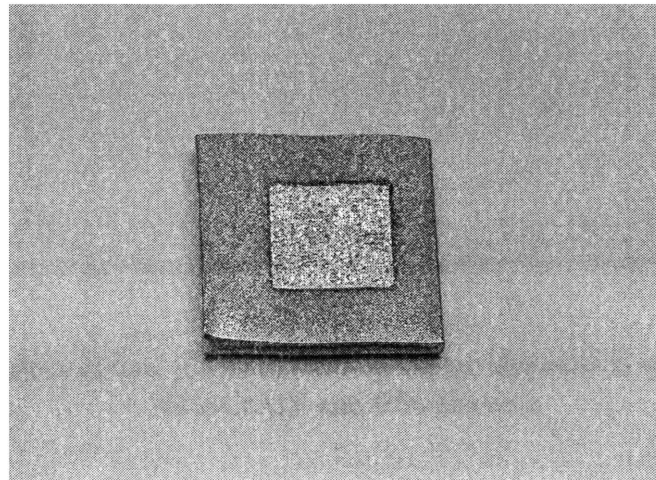
Figure 5.1. NiCoCrAlY bond coat

5.1.1. Main Effects. The main effects are plotted showing the influence of each factor on the surface deposition quality.

5.1.1.1 Overlap. The increase in overlap improves the deposition quality. As seen in Figure 5.2, the effect of change in overlap over the deposition quality causes decrease in surface roughness with increase in the overlap. The Y axis represents the surface roughness in micro inches while the X axis represents the two levels of the overlap.
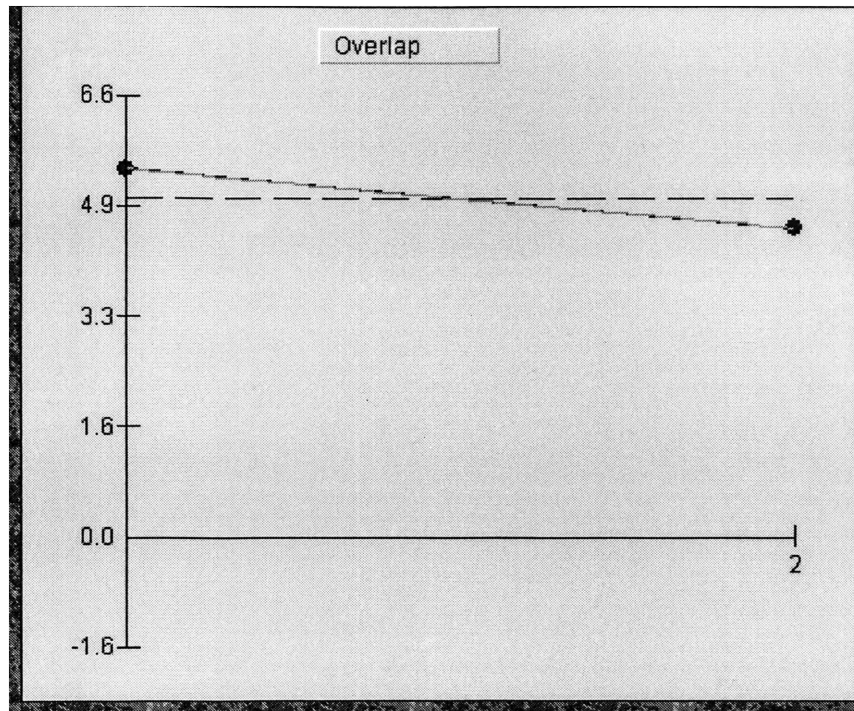
Figure 5.2. Effect of two levels of overlap on the deposition quality of 100 %
NiCoCrAlY and 0 % zirconia

5.1.1.2 Power. As seen in Figure 5.3, increasing the power decreases the surface quality as NiCoCrAlY has lower melting point. The Y axis represents the surface roughness in micro inches while the X axis represents the two levels of the power.

5.1.1.3 Inner gas. As seen in Figure 5.4, increasing the inner gas pressure increases the deposition quality. The Y axis represents the surface roughness in micro inches while the X axis represents the two levels of the inner gas pressure.

5.1.2. ANOVA. As seen in Figure 5.5, overlap and power are the most significant factors. The error includes the factor influence of all the interactions which are not taken into account. The factor influence of each interaction is always less than the influence of individual factors.
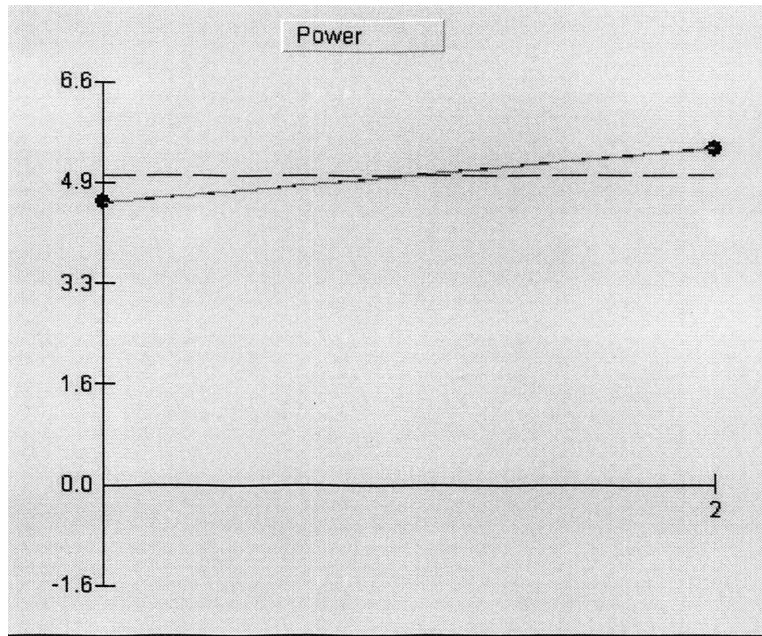
Figure 5.3. Effect of two levels of power on the deposition quality of 100 % NiCoCrAlY and 0 % zirconia
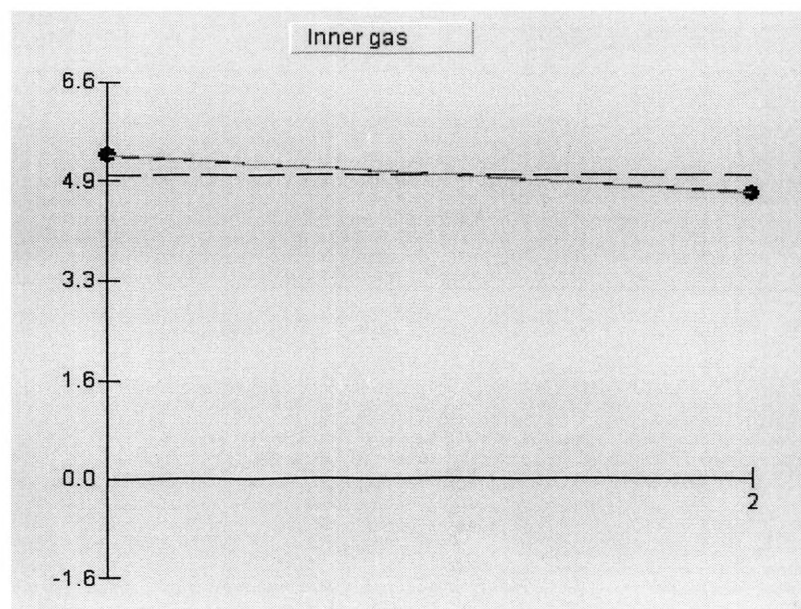

Figure 5.4. Effect of two levels of inner gas on the deposition quality of 100 % NiCoCrAlY and 0 % zirconia

ANOVA Table					Qualitek-4	_ □ ×

Expt File: 1000.Q4W   Data Type: Average Value   Print   Ok
QC Type: Smaller is Better   Help   Cancel

Col # / Factor	DOF (f)	Sum of Sqrs. (S)	Variance (V)	F - Ratio (F)	Pure Sum (S')	Percent P(%)
3 Overlap	1	2.253	2.253	8.722	1.994	27.606
4 Feedrate	1	.213	.213	.825	0	0
6 Power	1	2.253	2.253	8.722	1.995	27.606
8 Outer gas pressur	1	.213	.213	.825	0	0
9 Powder flow rate	1	.003	.003	.012	0	0
10 Inner gas	1	1.203	1.203	4.657	.944	13.076
11 Standoff distance	1	.053	.053	.206	0	0
Other/Error	4	1.032	.258			31.712
Total:	11	7.226				100.00%

Main Effects   Pool Factor   Auto Pool   Unpool All   CI Function   Bar Graph   Pie Chart   Optimum

Figure 5.5. ANOVA table showing relative influence of each factor

5.1.3. Optimum Conditions. The Table 5.1 shows the optimum conditions for the 100 % NiCoCrAlY and 0 % zirconia layer deposition. As NiCoCrAlY has a lower melting point the optimum values for most of the factors are level 1 values resulting in lower values of power intensity.

Table 5.1. Optimum conditions for 100 % NiCoCrAlY and 0 % zirconia.

Factors	Factor level
Overlap	0.45
Feed rate	20 IPM
Power	500 W
Outer gas Pressure	12 PSI
Powder flow rate	Low
Inner gas Pressure	6 PSI
Standoff distance	0.35 inches

5.2. 80 % NiCoCrAlY AND 20 % ZIRCONIA

The deposition consisted of 1 layer of 100% NiCoCrAlY and a top layer of 80% NiCoCrAlY and 20 % zirconia. The bottom layer was deposited using the optimum parameters obtained from the optimization of 100% NiCoCrAlY layer. As seen in the Figure 5.6, the deposition obtained for 80% NiCoCrAlY and 20% zirconia has higher surface roughness as compared to the 100% NiCoCrAlY layer.
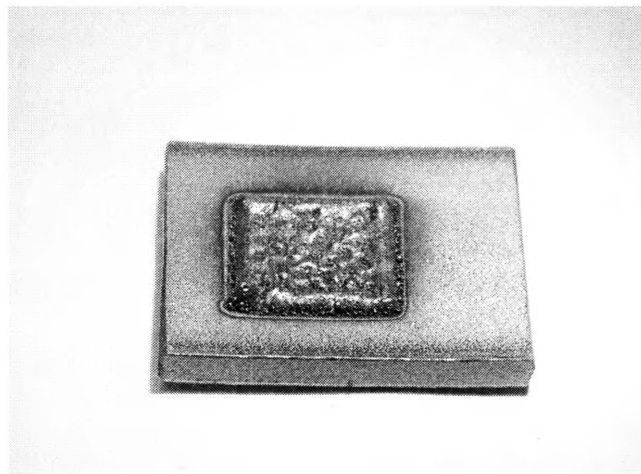
Figure 5.6. FGM with top layer of 80% NiCoCrAlY and 20% zirconia

5.2.1. Main Effects. The main effects for the control factors are plotted for the 80% NiCoCrAlY and 20% zirconia layer.

5.2.1.1 Overlap. As seen in Figure 5.7, the surface deposition quality increases with increase in the overlap factor. The Y axis represents the surface roughness in terms of overall evaluation criterion while the X axis represents the two levels of the overlap.

5.2.1.2 Feedrate. As seen in Figure 5.8, the quality of surface of the deposition decreases with increase in the feedrate. The Y axis represents the surface roughness in terms of overall evaluation criterion while the X axis represents the two levels of the feedrate.
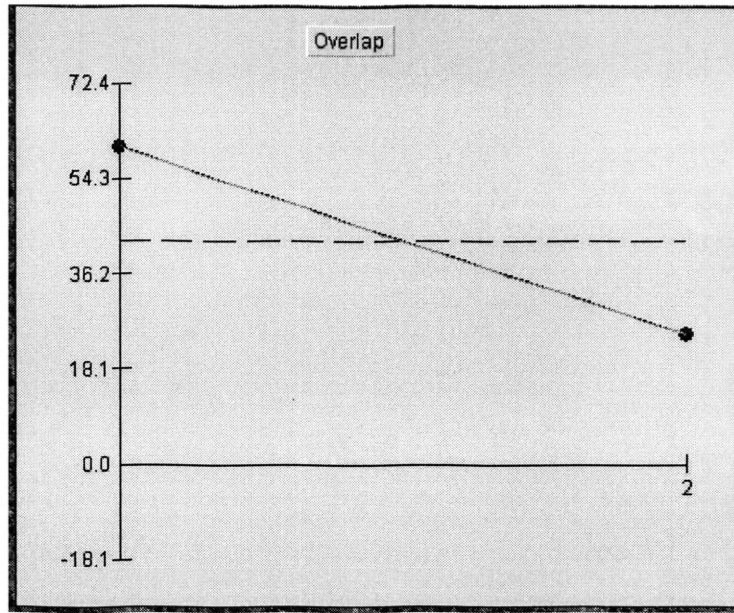
Figure 5.7. Effect of two levels of overlap on the deposition quality of 80 % NiCoCrAlY and 20 % zirconia
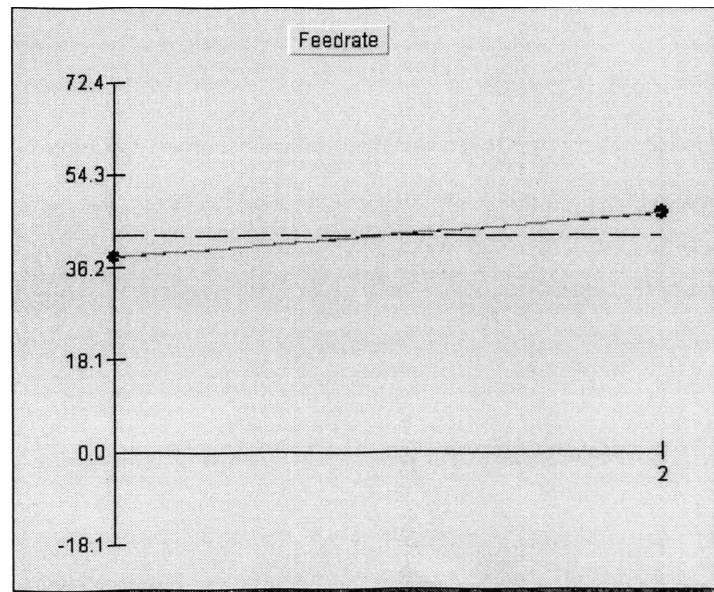
Figure 5.8. Effect of two levels of feed rate on the deposition quality of 80 % NiCoCrAlY and 20 % zirconia

5.2.1.3 Inner gas. As seen in Figure 5.9, the surface quality of the deposition increases with increase in the inner gas pressure. The Y axis represents the surface roughness in terms of overall evaluation criterion while the X axis represents the two levels of the inner gas.

Figure 5.9. Effect of two levels of inner gas on the deposition quality of 80 % NiCoCrAlY and 20 % zirconia

5.2.2. ANOVA. As seen in Figure 5.10, overlap and power are the main influencing factors. The error includes the factor influence of all the interactions which are not taken into account. The factor influence of each interaction is always less than the influence of individual factors. Here overlap has the highest influence followed by power.

Figure 5.10. ANOVA table for 80 % NiCoCrAlY and 20 % zirconia

5.2.3. Optimum Conditions. The Table 5.2, shows the optimum conditions for 80 % NiCoCrAlY and 20 % zirconia layer. The standoff distance has decreased as compared to the 100% NiCoCrAlY layer. More powder goes into the melt pool at a standoff distance of 0.25 inches as compared to 0.35 inches.

Table 5.2. Optimum conditions for 80 % NiCoCrAlY and 20% zirconia

Factors	Factor level
Overlap	0.45
Feed rate	20 IPM
Power	500 W
Outer gas Pressure	12 PSI
Powder flow rate	Low
Inner gas Pressure	6 PSI
Standoff distance	0.25 inches

5.3. 60 % NiCoCrAlY AND 40 % ZIRCONIA

       The deposition consists of three layers. The bottom layer of 100% NiCoCrAlY, the middle layer of 80% NiCoCrAlY and 20% zirconia and the top layer of 60% NiCoCrAlY and 40% zirconia. As seen in the Figure 5.11, the color of the deposition changes to black as the percentage of zirconia in the deposition is increased.
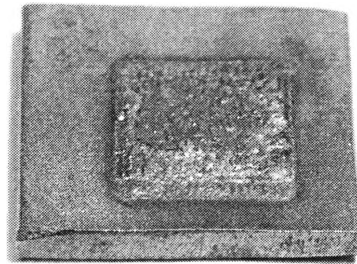
Figure 5.11. FGM with top layer of 60% NiCoCrAlY and 40% zirconia

       5.3.1. Main Effects. The main effects for the control factors are plotted for the 60% NiCoCrAlY and 40% zirconia layer.

       5.3.1.1 Power. As seen in Figure 5.12, surface roughness decreases with increase in the power.   With increase in the zirconia content the required power to melt the powder increases due to increase in the required energy intensity. The Y axis represents the surface roughness in terms of overall evaluation criterion while the X axis represents the two levels of the power.
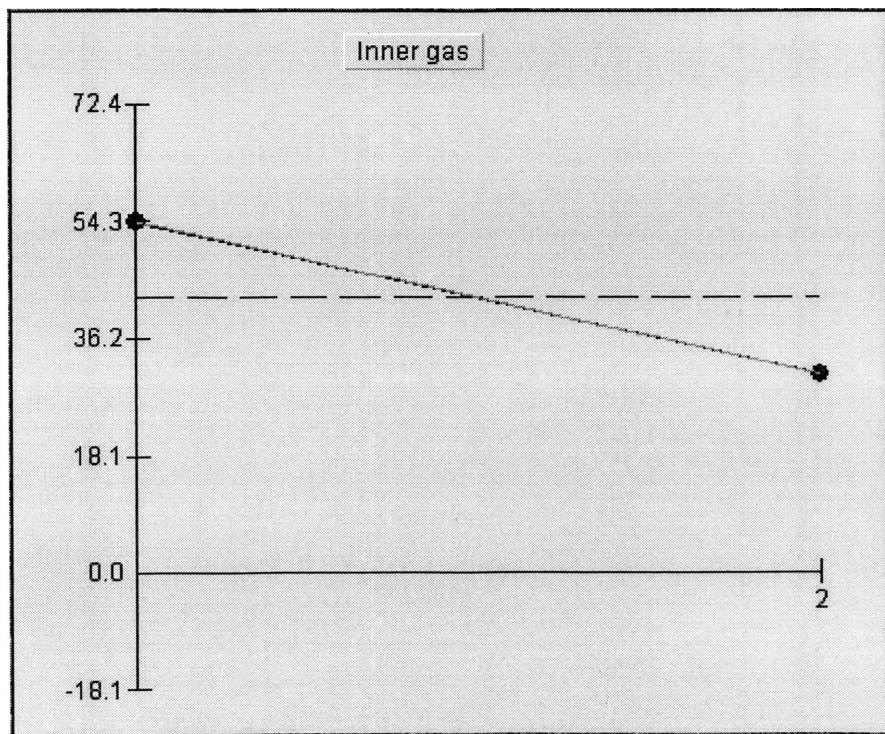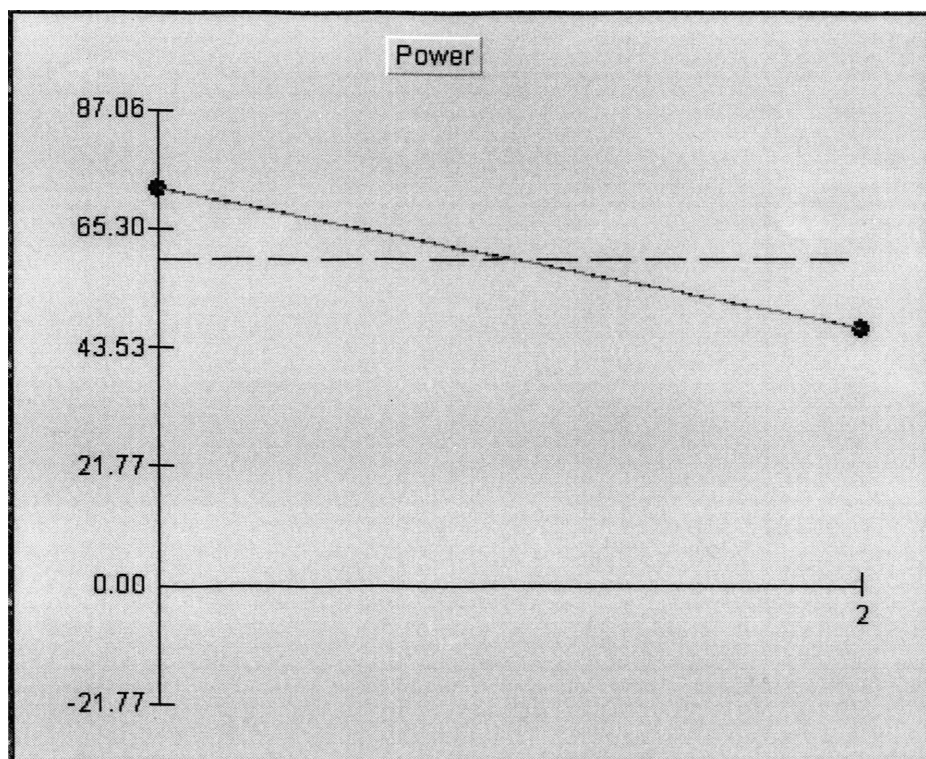
Figure 5.12. Effect of two levels of power on the deposition quality of 60 % NiCoCrAlY
and 40 % zirconia

5.3.1.2 Outer gas pressure. As seen in Figure 5.13, deposition surface quality improves with increase in outer gas pressure. This is due to the effect the gas pressure has on the powder accumulation in the melt pool. The Y axis represents the surface roughness while the X axis represents the two levels of the outer gas pressure.

5.3.1.3 Inner gas. As seen in Figure 5.14, deposition surface quality improves with increase in inner gas pressure. The Y axis represents the surface roughness while the X axis represents the two levels of the inner gas pressure. With the increase in the inner gas pressure the powder accumulated in the melt pool decreases causing an increase in available energy density for the accumulated powder in the melt pool.
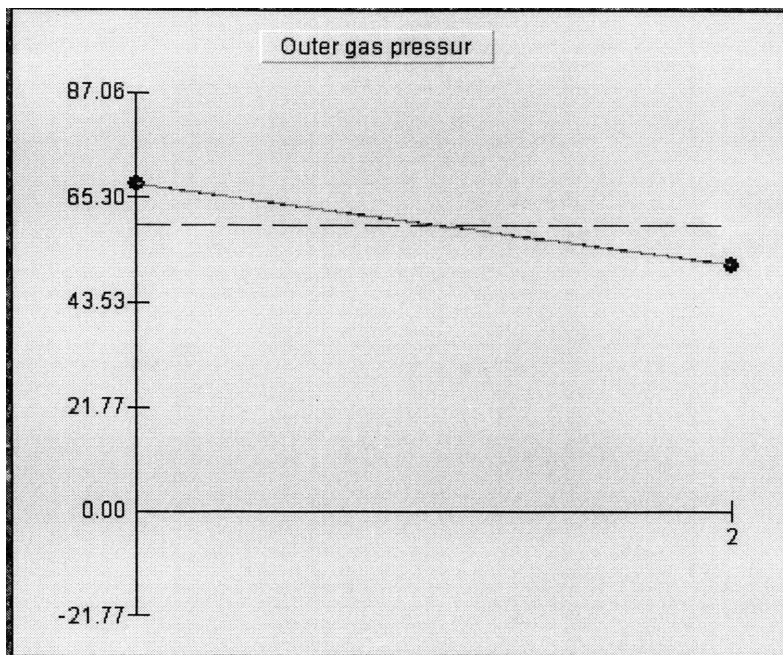
Figure 5.13. Effect of two levels of outer gas pressure on the deposition quality of 60 %
NiCoCrAlY and 40 % zirconia
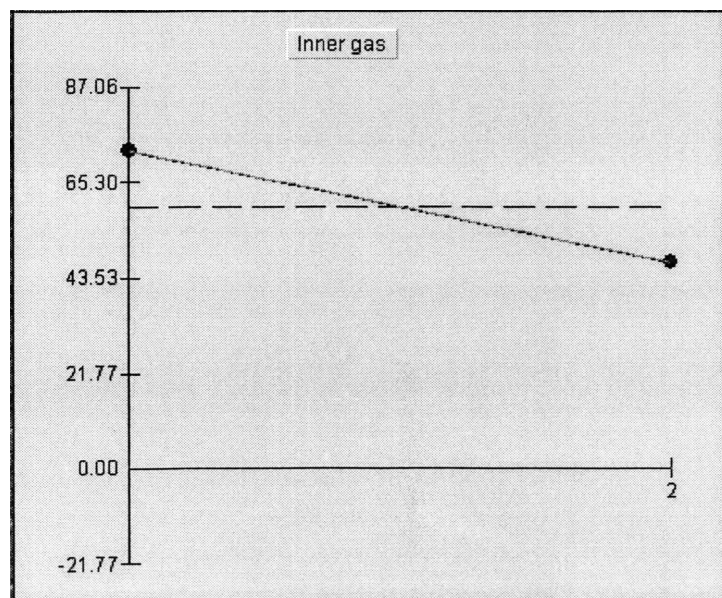
Figure 5.14. Effect of two levels of inner gas on the deposition quality of 60 %
NiCoCrAlY and 40 % zirconia

5.3.2. ANOVA. As seen in Figure 5.15, power and inner gas pressure are the most significant factors. The error includes the factor influence of all the interactions which are not taken into account. The factor influence of each interaction is always less than the influence of individual factors.

|		DOF	Sum of Sqrs.	Variance	F - Ratio	Pure Sum	Percent
Col # / Factor		(f)	(S)	(V)	(F)	(S')	P(%)
3 Overlap		1	4.509	4.509	.009	0	0
4 Feedrate		1	1.688	1.688	.003	0	0
6 Power		1	5853.785	5853.785	12.807	5396.729	19.49
8 Outer gas pressur		1	2502.997	2502.997	5.476	2045.941	7.389
9 Powder flow rate		1	424.366	424.366	.928	0	0
10 Inner gas		1	5788.155	5788.155	12.663	5331.099	19.253
11 Standoff distance		1	315.416	315.416	.69	0	0
Other/Error		28	12797.577	457.056			53.868
Total:		35	27688.498				100.00%

ANOVA Table — Qualitek-4

Expt. File: 6040.Q4W   Data Type: Average Value   QC Type: Smaller is Better

Main Effects | Pool Factor | Auto Pool | Unpool All | CI Function | Bar Graph | Pie Chart | Optimum

Figure 5.15. ANOVA table for 60 % NiCoCrAlY and 40 % zirconia

5.3.3. Optimum Conditions. Table 5.3, gives the optimum conditions for the deposition of 60% NiCoCrAlY and 40 % zirconia. The optimum energy intensity increases with an increase in the zirconia content. The power increases, feedrate increases causing an increase in the available energy intensity in the melt pool. The optimum conditions are chosen so as to have minimum surface roughness giving good deposition quality.

Table 5.3. Optimum conditions for 60 % NiCoCrAlY and 40% zirconia

Factors	Factor level
Overlap	0.45
Feed rate	40 IPM
Power	700 W
Outer gas Pressure	12 PSI
Powder flow rate	Low
Inner gas Pressure	4 PSI
Standoff distance	0.25 inches

5.4. 40 % NiCoCrAlY AND 60 % ZIRCONIA

The deposition consists of 4 layers. The bottom layer of 100% NiCoCrAlY, the second layer of 80% NiCoCrAlY and 20% zirconia, the third layer of 60% NiCoCrAlY and 40% zirconia and the top layer of 40% NiCoCrAlY and 60% zirconia. As seen in the Figure 5.16, as the zirconia content in the deposition increases the heat input in the deposition increases causing the substrate to turn black.
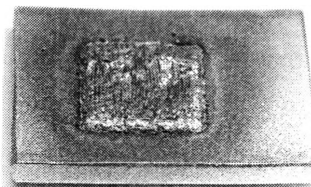
Figure 5.16. FGM with top layer of 40% NiCoCrAlY and 60% zirconia

5.4.1. Main Effects. The main effects for the control factors are plotted for the 40% NiCoCrAlY and 60% zirconia layer.

5.4.1.1 Feedrate. As seen in Figure 5.17, the surface quality of the deposition improves with increase in the feedrate. The Y axis represents the surface roughness in terms of overall evaluation criterion while the X axis represents the two levels of the feedrate.
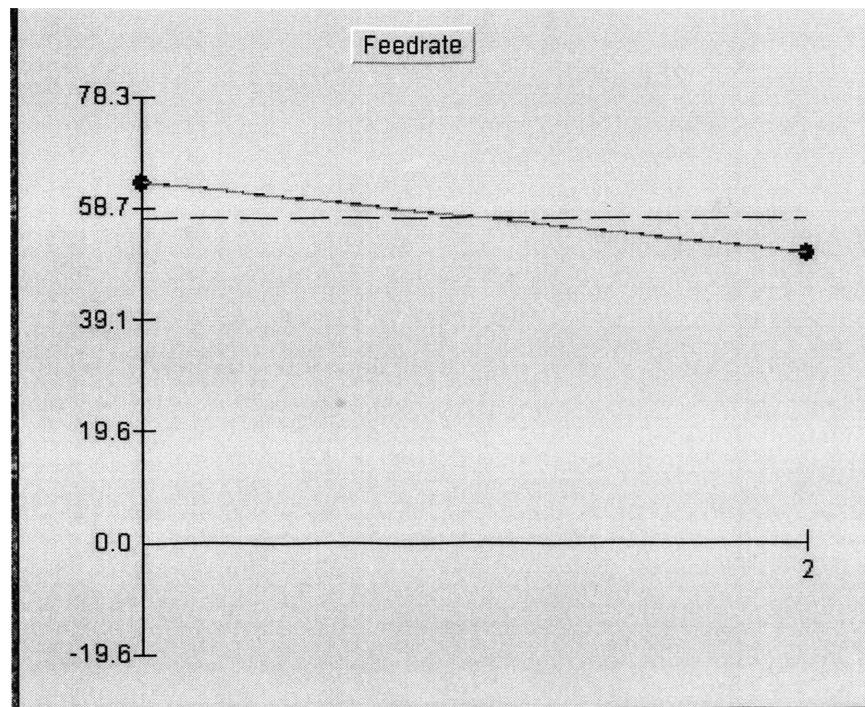
Figure 5.17. Effect of two levels of feed rate on the deposition quality of 40 % NiCoCrAlY and 60 % zirconia

5.4.1.2 Outer gas pressure. As seen in the Figure 5.18, the surface roughness decreases with increase in the outer gas pressure. The Y axis represents the surface roughness in terms of overall evaluation criterion while the X axis represents the two levels of the outer gas pressure.
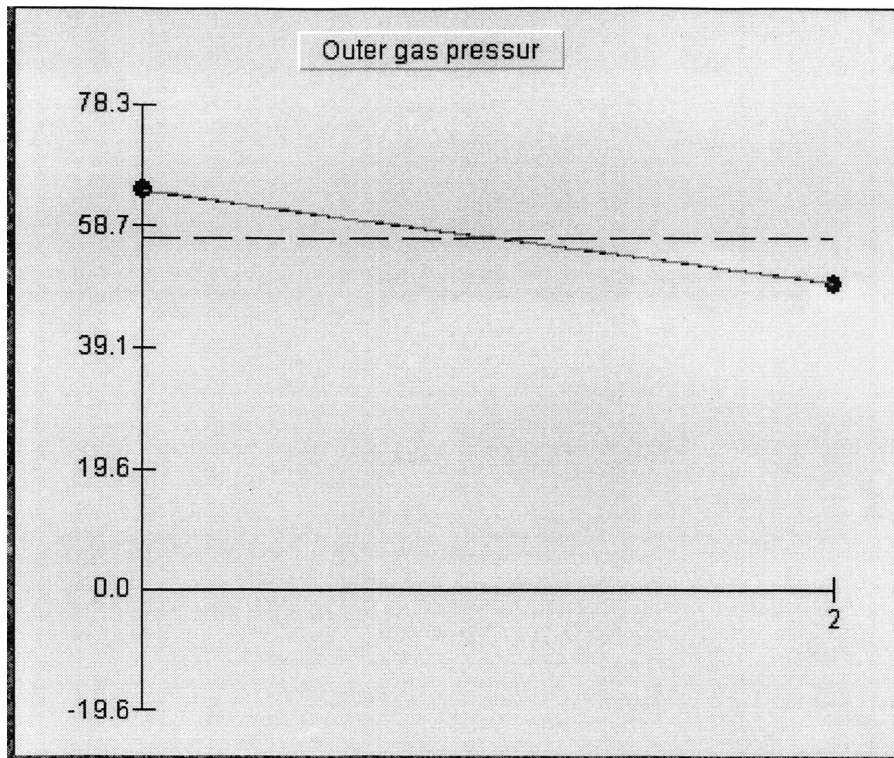
Figure 5.18. Effect of two levels of outer gas pressure on the deposition quality of 40 % NiCoCrAlY and 60 % zirconia

5.4.1.3 Inner gas. As seen in the Figure 5.19, the deposition surface quality increases with the increase in the inner gas pressure. The Y axis represents the surface roughness in terms of overall evaluation criterion while the X axis represents the two levels of the inner gas pressure.

5.4.2. ANOVA. As seen in the Figure 5.20, standoff distance and outer gas pressure are the most significant factors for the deposition of 40% NiCoCrAlY and 60% zirconia layer. The error includes the factor influence of all the interactions which are not taken into account. The factor influence of each interaction is always less than the influence of individual factors.

Figure 5.19. Effect of two levels of inner gas pressure on the deposition quality of 40 %
NiCoCrAlY and 60 % zirconia

Figure 5.20. ANOVA table for 40 % NiCoCrAlY and 60 % zirconia

5.4.3. Optimum Conditions. The optimum condition values for different factors are shown in the Table 5.4. The optimum energy intensity increases with an increase in the zirconia content.

Table 5.4. Optimum conditions for 40 % NiCoCrAlY and 60 % zirconia

Factors	Factor level
Overlap	0.45
Feed rate	40 IPM
Power	700 W
Outer gas Pressure	12 PSI
Powder flow rate	Low
Inner gas Pressure	6 PSI
Standoff distance	0.25 inches

5.5. 20 % NiCoCrAlY AND 80 % ZIRCONIA

The deposition consists of five layers with the topmost layer consisting of 20% NiCoCrAlY and 80% zirconia. As seen in the Figure 5.21, the deposition sample for the optimum deposition conditions for 20% NiCoCrAlY and 80% zirconia is shown.

5.5.1. Main Effects. The main effects for the control factors are plotted for the 20% NiCoCrAlY and 80% zirconia layer for feedrate, power, outer gas pressure and inner gas pressure.

5.5.1.1 Feedrate. As seen in the Figure 5.22, the surface roughness of the deposition decreases with increase in the feedrate. The Y axis represents the surface roughness in terms of overall evaluation criterion while the X axis represents the two levels of the feedrate.
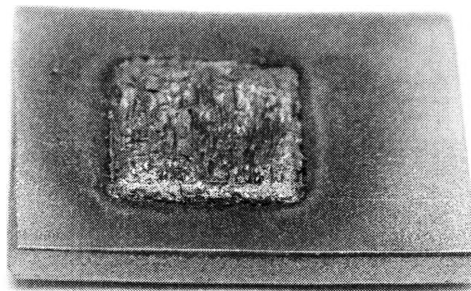
Figure 5 21. FGM layer with top layer of 20% NiCoCrAlY and 80% zirconia
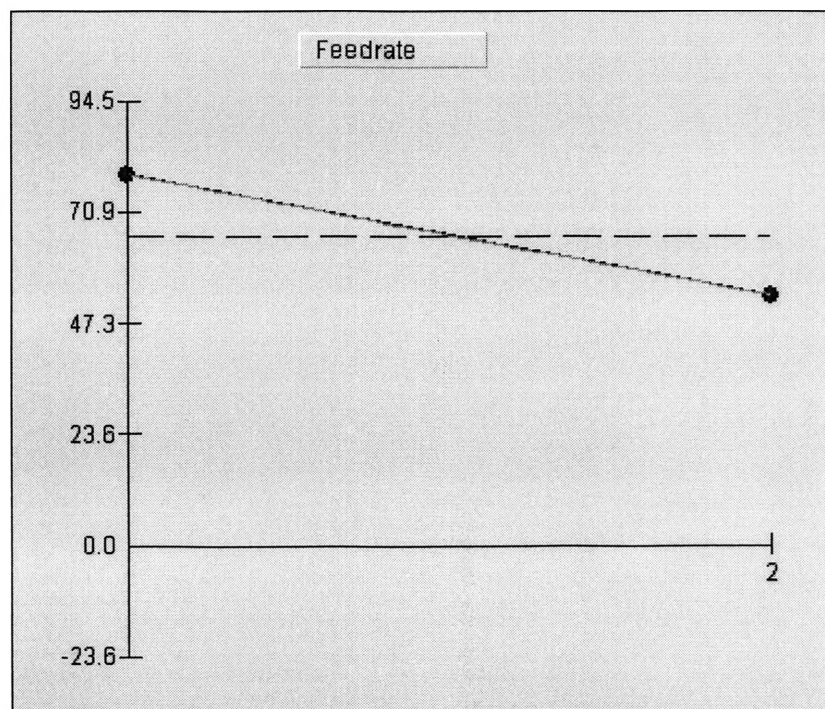
Figure 5.22. Effect of two levels of feed rate on the deposition quality of 20 %
NiCoCrAlY and 80 % zirconia

5.5.1.2 Power. As seen in the Figure 5.23, the surface quality of deposition increases with increase in the power. The Y axis represents the surface roughness in terms of overall evaluation criterion while the X axis represents the two levels of the power.
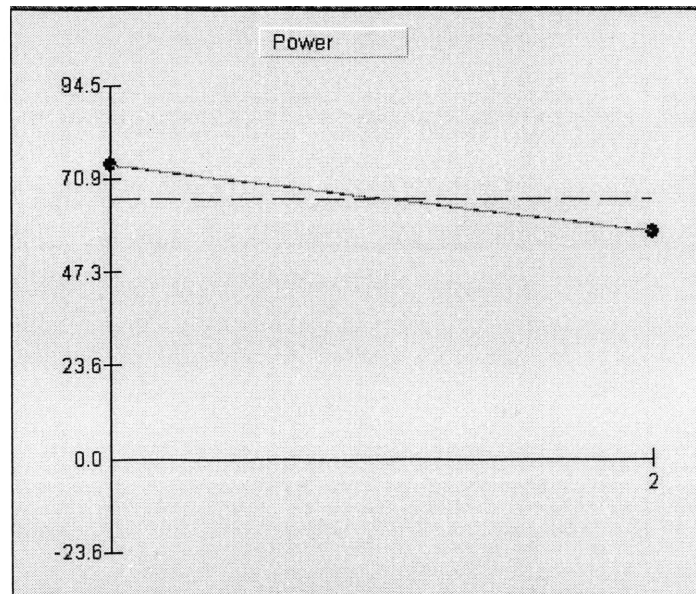
Figure 5.23. Effect of two levels of power on the deposition quality of 20 % NiCoCrAlY and 80 % zirconia

5.5.1.3 Outer gas pressure. As seen in the Figure 5.24, the surface quality of deposition improves with increase in the outer gas pressure. The Y axis represents the surface roughness in terms of overall evaluation criterion while the X axis represents the two levels of the outer gas pressure.

5.5.1.4 Inner gas. As seen in the Figure 5.25, the surface roughness decreases with increase in the inner gas pressure. The Y axis represents the surface roughness in while the X axis represents the two levels of the inner gas pressure.

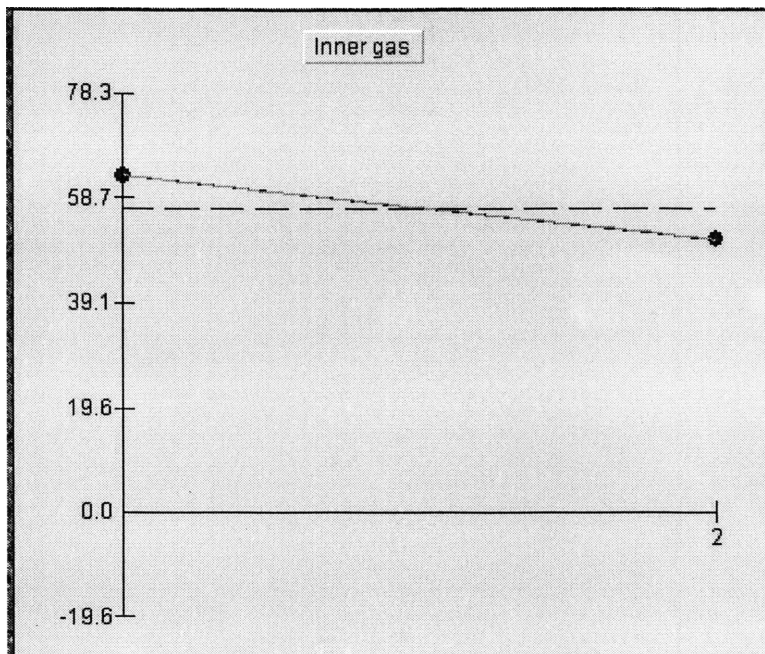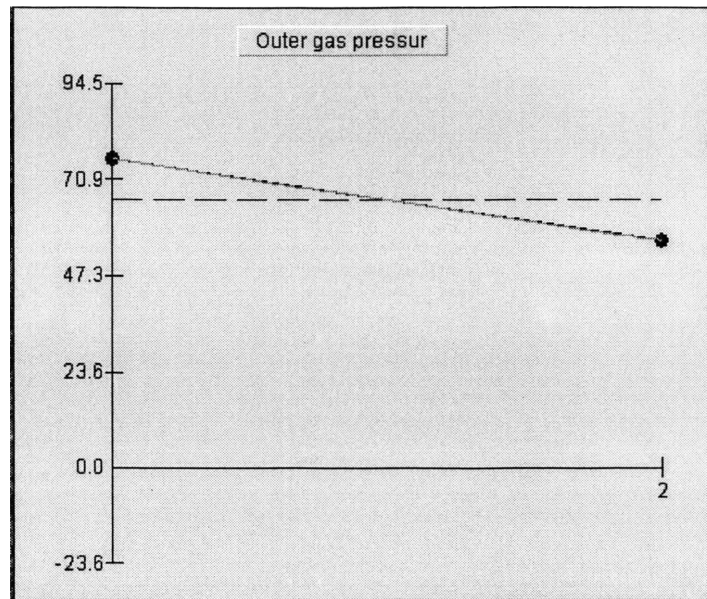Figure 5.24. Effect of two levels of outer gas pressure on the deposition quality of 20 % NiCoCrAlY and 80 % zirconia

Figure 5.25. Effect of two levels of inner gas pressure on the deposition quality of 20 % NiCoCrAlY and 80 % zirconia

5.5.2. ANOVA. As seen in the Figure 5.26, standoff distance plays a dominating role 20% NiCoCrAlY and 0% zirconia layer. The error includes the factor influence of all the interactions which are not taken into account. The factor influence of each interaction is always less than the influence of individual factors. The standoff distance has the maximum effect as the percentage of powder falling in the melt pool varies with the stand off distance.

Col # / Factor	DOF (f)	Sum of Sqrs. (S)	Variance (V)	F - Ratio (F)	Pure Sum (S')	Percent P(%)
3 Overlap	1	292.356	292.356	2.305	165.557	1.438
4 Feedrate	1	1384.951	1384.951	10.922	1258.152	10.929
6 Power	1	209.803	209.803	1.654	83.004	.721
8 Outer gas pressur	1	2022.444	2022.444	15.95	1895.645	16.467
9 Powder flow rate	1	323.928	323.928	2.554	197.129	1.712
10 Inner gas	1	1278.185	1278.185	10.08	1151.386	10.002
11 Standoff distance	1	2449.105	2449.105	19.314	2322.306	20.174
Other/Error	28	3550.372	126.799			38.557
Total:	35	11511.148				100.00%

ANOVA Table — Qualitek-4

Expt. File: 40d0.Q4W   Data Type: Average Value   QC Type: Smaller is Better

Print   Ok   Help   Cancel

Main Effects | Pool Factor | Auto Pool | Unpool All | CI Function | Bar Graph | Pie Chart | Optimum

Figure 5.26. ANOVA table for 20 % NiCoCrAlY and 80 % zirconia

5.5.3. Optimum Conditions. As seen in the Table 5.5, are the optimum conditions for 20% NiCoCrAlY and 100% zirconia layer. The optimum energy intensity increases with an increase in the zirconia content. The power increases, feedrate increases causing an increase in the available energy intensity in the melt pool.

Table 5.5. Optimum conditions for 20 % NiCoCrAlY and 80% zirconia

Factors	Factor level
Overlap	0.25
Feed rate	40 IPM
Power	700 W
Outer gas Pressure	12 PSI
Powder flow rate	Low
Inner gas Pressure	6 PSI
Standoff distance	0.25 inches

5.6. 0 % NiCoCrAlY AND 100 % ZIRCONIA

The deposition consists of six layers with the top layer consisting of 100% zirconia. As seen in the Figure 5.27, the deposition sample for the optimum conditions for 100% zirconia layer is shown with zirconia layer being the top layer of the deposition.
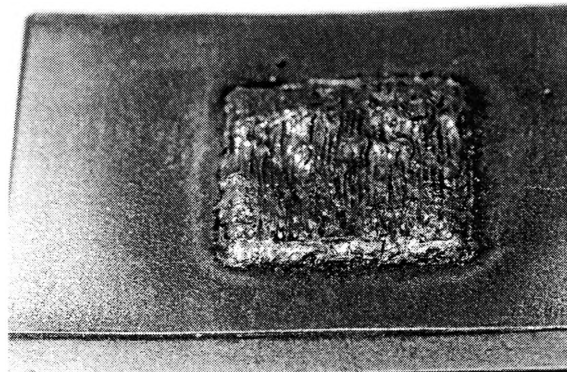
Figure 5.27. FGM layer with top layer 0%NiCoCrAlY and 100%zirconia

5.6.1. Main Effects. The main effects for the control factors are plotted for the 0% NiCoCrAlY and 100% zirconia layer.

5.6.1.1 Feedrate. As seen in the Figure 5.28, the surface roughness decreases with increase in the feedrate 100% zirconia layer. The Y axis represents the surface roughness while the X axis represents the two levels of the feedrate.
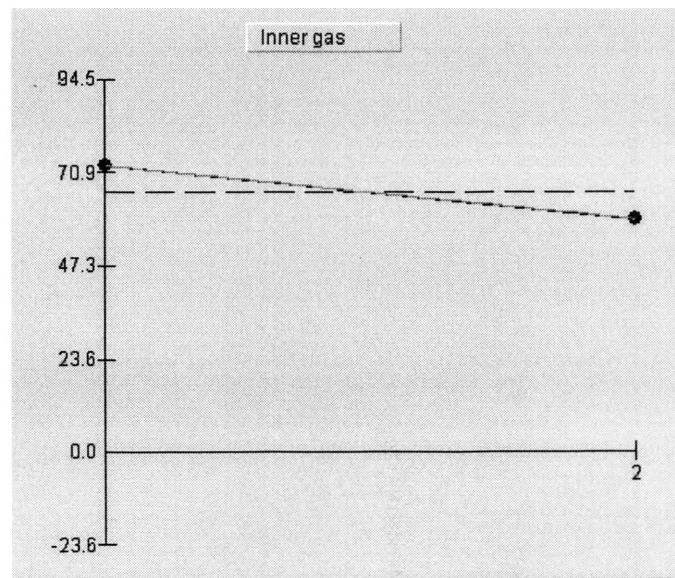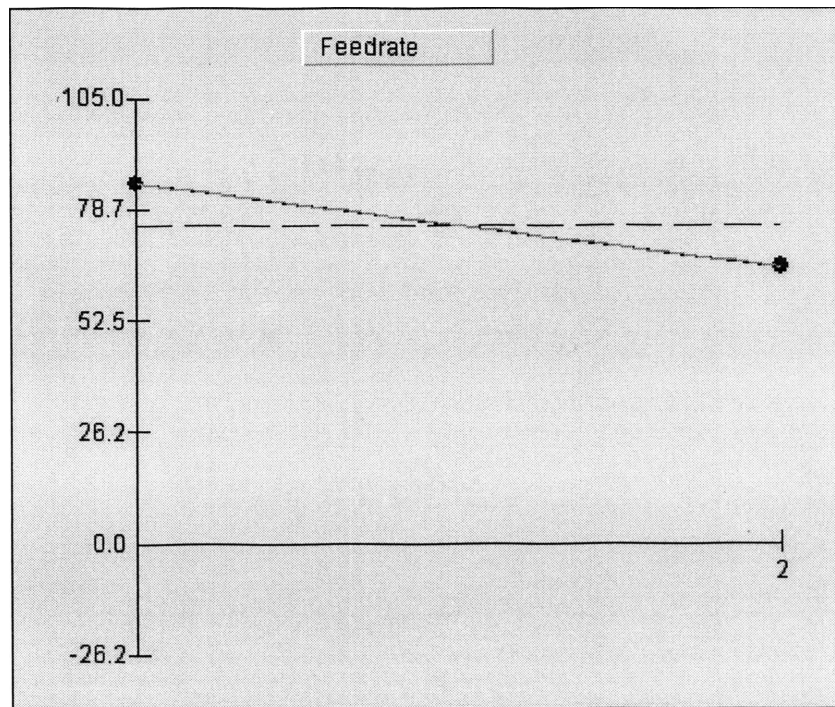

Figure 5.28. Effect of two levels of feed rate on the deposition quality of 0 % NiCoCrAlY and 100 % zirconia

5.6.1.2 Power. As seen in the Figure 5.29, the surface roughness of the deposition decreases with increase in the power used for the deposition. The Y axis represents the surface roughness in terms of overall evaluation criterion while the X axis represents the two levels of the power.
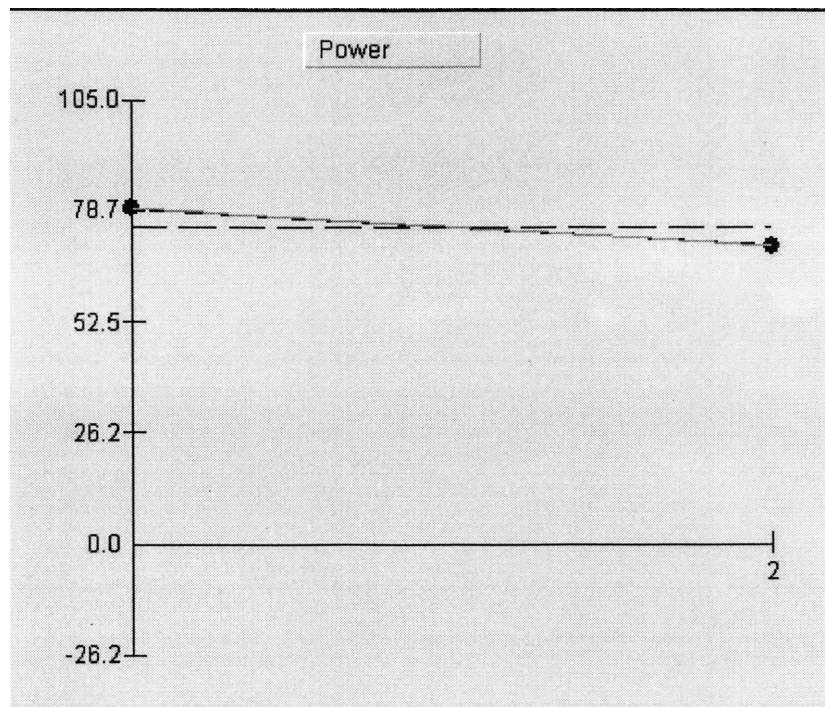
Figure 5.29. Effect of two levels of power on the deposition quality of 0 % NiCoCrAlY and 100 % zirconia

5.6.1.3 Outer gas pressure. As seen in the Figure 5.30, the surface roughness of the deposition layers decreases with increase in the outer gas pressure used for the deposition. The Y axis represents the surface roughness in terms of overall evaluation criterion while the X axis represents the two levels of the outer gas pressure.

5.6.1.4 Inner gas. As seen in Figure 5.31, the surface quality of deposition increases with increase in the inner gas pressure for 100 % zirconia layer. The Y axis represents the surface roughness while the X axis represents the two levels of inner gas pressure.

5.6.2. ANOVA. As seen in the Figure 5.32, the standoff distance and the outer gas pressure is the influencing factors for 100% zirconia deposition. The error includes the factor influence of all the interactions which are not taken into account. The factor influence of each interaction is always less than the influence of individual factors.
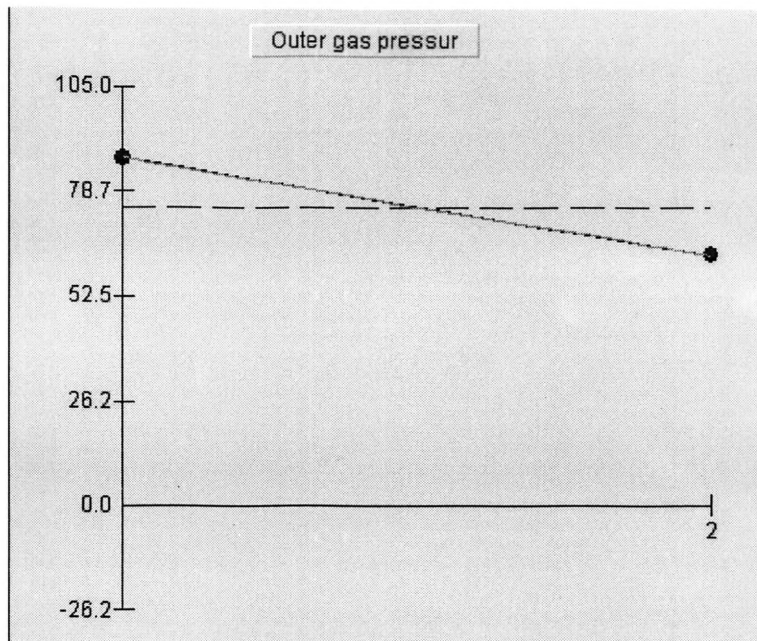
Figure 5.30. Effect of two levels of outer gas pressure on the deposition quality of 0 % NiCoCrAlY and 100 % zirconia

Figure 5.31. Effect of two levels of inner gas pressure on the deposition quality of 0 % NiCoCrAlY and 100 % zirconia

Col # / Factor	DOF (f)	Sum of Sqrs. (S)	Variance (V)	F - Ratio (F)	Pure Sum (S')	Percent P(%)
3 Overlap	1	440.922	440.922	1.105	42.106	.554
4 Feedrate	1	1181.27	1181.27	2.961	782.453	10.311
6 Power	1	239.946	239.946	.601	0	0
8 Outer gas pressur	1	1765.15	1765.15	4.425	1366.334	18.005
9 Powder flow rate	1	39.086	39.086	.098	0	0
10 Inner gas	1	435.122	435.122	1.091	36.305	.478
11 Standoff distance	1	1891.532	1891.532	4.742	1492.715	19.671
Other/Error	4	1595.264	398.816			50.981
Total:	11	7588.297				100.00%

Figure 5.32. ANOVA table for 0 % NiCoCrAlY and 100 % zirconia

5.6.3. Optimum Conditions. As seen in the Table 5.6, the optimum conditions for the 100% zirconia deposition are shown. The optimum energy intensity increases with an increase in the zirconia content.

Table 5.6. Optimum conditions for 0 % NiCoCrAlY and 100% zirconia

Factors	Factor level
Overlap	0.25
Feed rate	40 IPM
Power	700 W
Outer gas Pressure	12 PSI
Powder flow rate	Low
Inner gas Pressure	6 PSI
Standoff distance	0.25 inches

The experimental readings obtained for the two trials for each layer in the FGM are as shown in the Table 5.7. The surface roughness was measured in micro inches for each of the six different layers. Two readings were taken at each experimental setting for the six layers indicated as NiCoCrAlY percentage/ zirconia percentage. As the zirconia content increases the surface roughness increases. 8 micro inches was the maximum surface roughness measured within the range of the instrument.

Table 5.7. Experimental readings

100/0			80/20		60/40	
Setting	Trial 1	Trial 2	Trial 1	Trial 2	Trial 1	Trial 2
	Surface Roughness (μ in)		Surface Roughness (μ in)		Surface Roughness (μ in)	
1	3.51	3.87	5.27	5.87	7	7.14
2	3.23	3.48	5.65	5.84	4.1	4.54
3	4.56	5.12	6.12	5.95	5.91	6.02
4	4.81	5.65	8	8.25	5.13	5.24
5	3.12	3.58	4.63	4.82	4.39	4.65
6	5	5.48	5.75	5.14	5.78	5.12
7	4.73	5.01	6.03	6.41	5.44	5.21
8	4.97	5.24	4.16	4.74	6.4	5.98
9	4.15	4.35	8	8.45	6.01	6.48
10	3.89	4.12	4.11	4.32	5.2	5.78
11	5.57	5.01	5.69	5.84	4.95	5.12
12	4.31	4.47	5.6	5.98	4.4	4.65

Table 5.7. Experimental readings (cont)

40/60			20/80		0/100	
Setting	Trial 1	Trial 2	Trial 1	Trial 2	Trial 1	Trial 2
	Surface Roughness (μ in)		Surface Roughness (μ in)		Surface Roughness (μ in)	
1	5.71	5.98	6.05	6.47	7	6.24
2	4.9	5.12	5.67	6.01	5.41	5.87
3	5.31	5.95	5.15	5.47	5.95	5.26
4	6.1	6.45	4.99	5.14	7	6.49
5	5.1	5.14	3.52	3.95	4.54	4.89
6	6.19	5.84	5.26	5.76	6.25	6.74
7	4.39	4.01	6.05	6.48	6.36	6.56
8	5.5	5.88	5.8	5.92	5.77	5.25
9	6.08	6.74	7	6.14	6.58	6.87
10	5.78	5.55	5.8	5.11	5.91	5.14
11	5.03	5.45	5.4	6.01	5.15	5.76
12	5.99	5.44	6.01	5.47	5.24	5.74

5.7. RESIDUAL STRESS ANALYSIS

Rapid heating and cooling of the deposited material cause accumulation of stresses in the deposition. A crucial aspect is the nature and distribution of internal residual stresses. For example, compressive stresses tend to close microcracks directing perpendicular to the surface of the coating. Strong tensile residual stresses on the other hand may lead to a complete detachment of the coating. Knowledge of residual stress profiles allows optimizing the deposition technique.

The TBC deposition was analyzed for residual stresses using x-ray copper source diffraction having a wavelength of 1.541 °A. Philips Xpert materials research

diffractometer operated in point focus mode. Incident beam optics used cross slit collimator having a slit height of 1 mm with incident beam area of 1 mm x 1 mm. Parallel plate collimator equipped with flat graphite monochromator was used on a (000) plane. The data angle range is 92.015° to 97.985° with a scan step size of 0.03° with a sample of 200 points for each of the points plotted on the $d - \sin^2\psi$ graph.

The results show a compressive residual stress of 39.1 MPa (Figure 5.40). This can be compared with the literature values of residual stress in the TBC and Thermally Grown Oxide (TGO) layers of 70MPa and 3.5GPa [15]. This makes LAMP a potential candidate for TBC deposition. The compressive residual stress increases the tensile stress value at which the failure occurs as the initial operational tensile stress is negated by the compressive residual stress. Thus LAMP process seems to give better residual stress characteristics for the NiCoCrAlY and zirconia coating deposition. In the x-ray diffraction residual stress measurement the strain in the crystal lattice is measured, and the residual stress producing the stress is calculated, assuming a linear elastic distortion of the crystal lattice. As seen in Figure 5.33, the sample is titled through an angle ψ, to determine the residual stress.

The $\sin^2\psi$ technique of residual stress measurement by x-ray diffraction was used. The figure 5.33 shows the diffraction of a monochromatic beam of x-rays at a high diffraction angle 2θ from the surface of a stressed sample for two orientations of the sample relative to the x-ray beam. The angle ψ, defining the orientation of the sample surface, is the angle between the normal of the surface and the incident and diffracted beam bisector, which is also the angle between the normal to the diffracting lattice planes and the sample surface. Diffraction occurs at an angle 2θ defined by Bragg's Law: $n\lambda. = 2d \sin\theta$, where n is an integer denoting the order of diffraction, λ is the x-ray wavelength, d is the lattice spacing of crystal planes, and θ is the diffraction angle. For the monochromatic x-rays produced by the metallic target of an x-ray tube, the wavelength is known to 1 part in 10^5. Any change in the lattice spacing, d, results in a corresponding shift in the diffraction angle 2θ.

Figure 5.33(a) shows the sample in the $\psi = 0$ orientation. The presence of a tensile stress in the sample results in a Poisson's ratio contraction, reducing the lattice spacing and slightly increasing the diffraction angle, 2θ. If the sample is then rotated

through some known angle ψ (Fig. 5.33(b)), the tensile stress present in the surface increases the lattice spacing over the stress-free state and decreases 2θ.
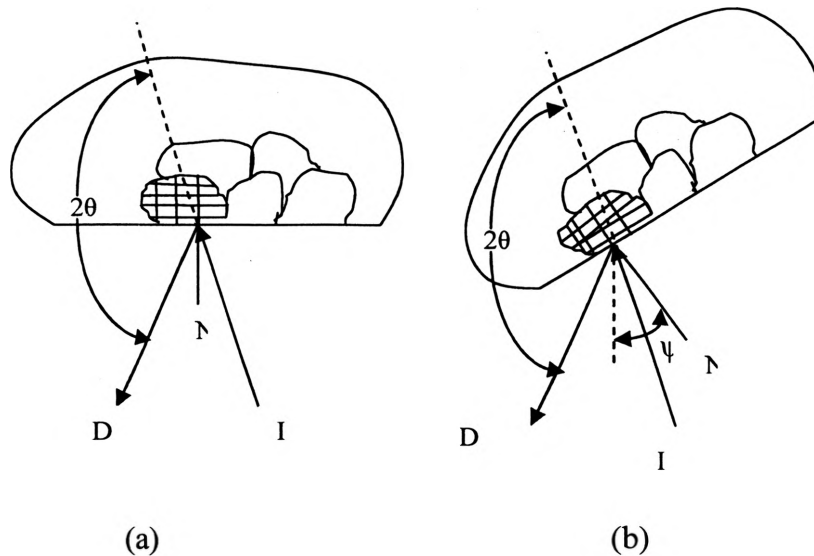

Figure 5.33. Setting for residual stress determination [16]

Measuring the change in the angular position of the diffraction peak for at least two orientations of the sample defined by the angle ψ enables calculation of the stress present in the sample surface lying in the plane of diffraction, which contains the incident and diffracted x-ray beams. To measure the stress in different directions at the same point, the sample is rotated about its surface normal to coincide the direction of interest with the diffraction plane.

X-ray diffraction stress measurement is confined to the surface of the sample. Electro polishing is used to expose new surfaces for subsurface measurement. That is, a stress distribution described by principal stresses σ_1 and σ_2 exists in the plane of the surface, and no stress is assumed perpendicular to the surface, $\sigma_3 = 0$. However, a strain component perpendicular to the surface ε_3 exists as a result of the Poisson's ratio contractions caused by the two principal stresses as seen in Figure 5.34.
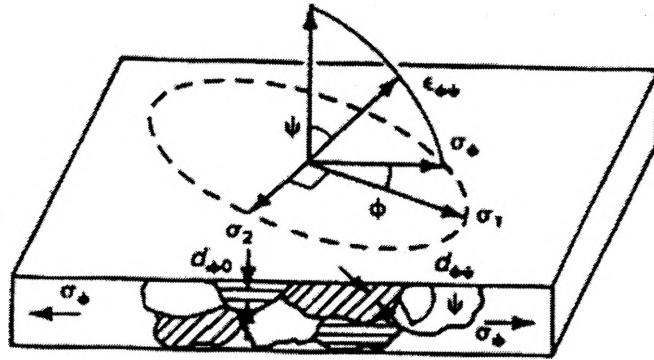
Figure 5.34. Plane-stress elastic model [16]

The strain ε defined in the directions θ and ψ is given by

$$\varepsilon_{\psi\varphi}= [((1+\upsilon)/E)(\sigma_1\alpha_1{}^2+\sigma_2\alpha_2{}^2)]-[(\upsilon/E)(\sigma_1+\sigma_2)] \tag{12}$$

Where E is the modulus of elasticity, ν is the Poisson's ratio and α_1 and α_2 are the angle cosines of the strain vector.

$$\varepsilon_{\psi\varphi}= [((1+\upsilon)/E)(\sigma_1\cos^2\varphi+\sigma_2\sin^2\varphi)\sin^2\psi]-[(\upsilon/E)(\sigma_1+\sigma_2)] \tag{13}$$

For $\psi=90^0$, stress vector $\sigma_\varphi = \sigma_1 \cos^2\varphi + \sigma_2 \sin^2\varphi$, thus the strain in terms of surface stress is given by,

$$\mathcal{E}_{\psi\varphi}= [((1+\upsilon)/E)\sigma_\varphi\sin^2\psi]-[(\upsilon/E)(\sigma_1+\sigma_2)] \, , \tag{14}$$

The strain in terms of changes in the dimensions of crystal lattice is given by,

$$\varepsilon_{\varphi\psi}=(d_{\varphi\psi} - d_0)/d_0 \, . \tag{15}$$

The lattice spacing for any direction is thus given by,

$$d_{\varphi\psi}=[((1+\upsilon)/E)\sigma_\varphi d_0\sin^2\psi]-[(\upsilon/E)d_0(\sigma_1+\sigma_2)+d_0] \, . \tag{16}$$

This equation defines the relationship between the lattice spacing and the biaxial stresses in the sample surface. The lattice spacing $d_{\varphi\psi}$ is a linear function of $\sin^2\psi$. The slope of the plot can be solved for surface stress which essentially is the residual stress to give the equation,

$$\sigma_\varphi = [E/(1+\nu)](1/d_0)(\partial d_{\varphi\psi}/\partial\sin^2\psi) \tag{17}$$

The x-ray elastic constants can be determined empirically, but the unstressed lattice spacing, d_0, is generally unknown. However, because $E \gg (s_1 + s_2)$, the value of $d\varphi_0$ differs from d_0 by not more than $\pm$ 1%, and may be approximated to this accuracy using:

$$\sigma_\varphi = [E/(1+\nu)](1/d_{\varphi 0})(\partial d_{\varphi\psi}/\partial \sin^2\psi). \tag{18}$$

This is a differential technique and no stress free samples are required to determine d_0 for the biaxial stress case.

In the technique used the lattice spacing is calculated for multiple values of ψ by tilting the sample to give a plot of lattice spacing and $\sin^2\psi$. This gives the surface stress in the sample.

The steps involved in the residual stress measurement are

Sample preparation

Sample positioning

Irradiation area and measurement time

Diffraction peak location

Precise location of the position of the diffraction peak which gives maximum intensity at each ψ tilt is determined in terms of θ to give the values of $d_{\varphi\psi}$ by Bragg's equation. Figure 5.35, Figure 5.36, Figure 5.37, Figure 5.38, Figure 5.39 give the intensity distribution for five different values of ψ and the peak of each distribution corresponds to the 2θ values used to calculate d, the lattice spacing, corresponding to the values used for the residual stress calculation in the d- $\sin^2\psi$ graph in the Figure 5.40.

As seen in Figure 5.35, the peak of the intensity -2Theta distribution gives the value of 2Theta used in calculating the d spacing.

As seen in Figure 5.35, the intensity-2theta distribution is plotted to determine the peak position for ψ=0. As seen in Figure 5.36, the intensity-2theta distribution is plotted to determine the peak position for ψ=28.02. The intensity of the refracted radiation is plotted on the Y axis while the angle of refraction is plotted on the X axis.

As seen in Figure 5.37, the intensity-2theta distribution is plotted to determine the peak position for ψ=41.64. The intensity of the refracted radiation is plotted on the Y axis while the angle of refraction is plotted on the X axis.

As seen in Figure 5.38, the intensity-2theta distribution is plotted to determine the peak position for ψ=54.47. The intensity of the refracted radiation is plotted on the Y axis while the angle of refraction is plotted on the X axis.

Figure 5.35. 2 θ- intensity distribution for ψ =0

Figure 5.36. 2 θ- intensity distribution for ψ = 28.02

Figure 5.37. 2 θ- intensity distribution for ψ =41.64
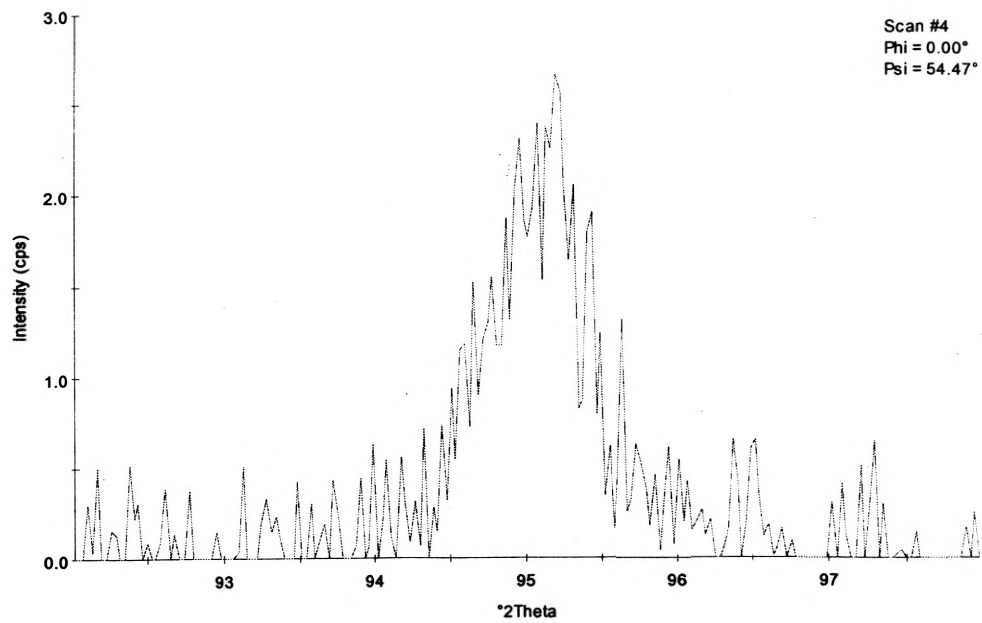
Figure 5.38. 2 θ- intensity distribution for ψ =54.47

With increase in the Psi value the distribution broadens. As seen in Figure 5.39, the intensity-2theta distribution is plotted to determine the peak position for ψ=70. The intensity of the refracted radiation is plotted on the Y axis while the angle of refraction is plotted on the X axis.
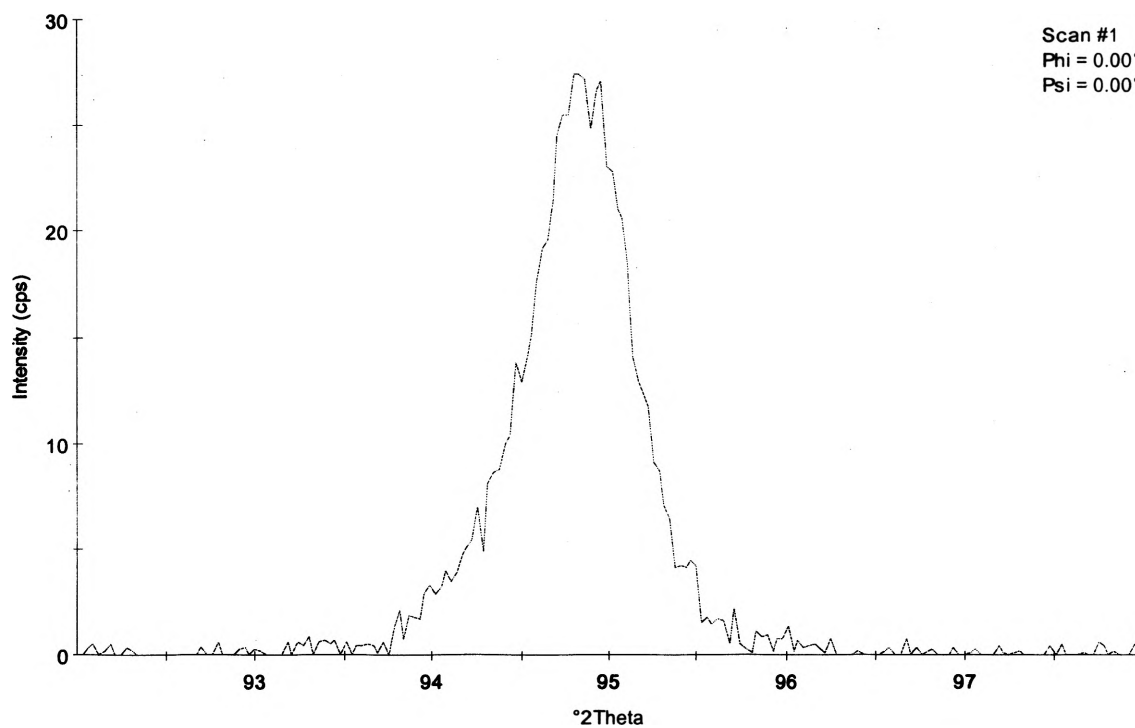

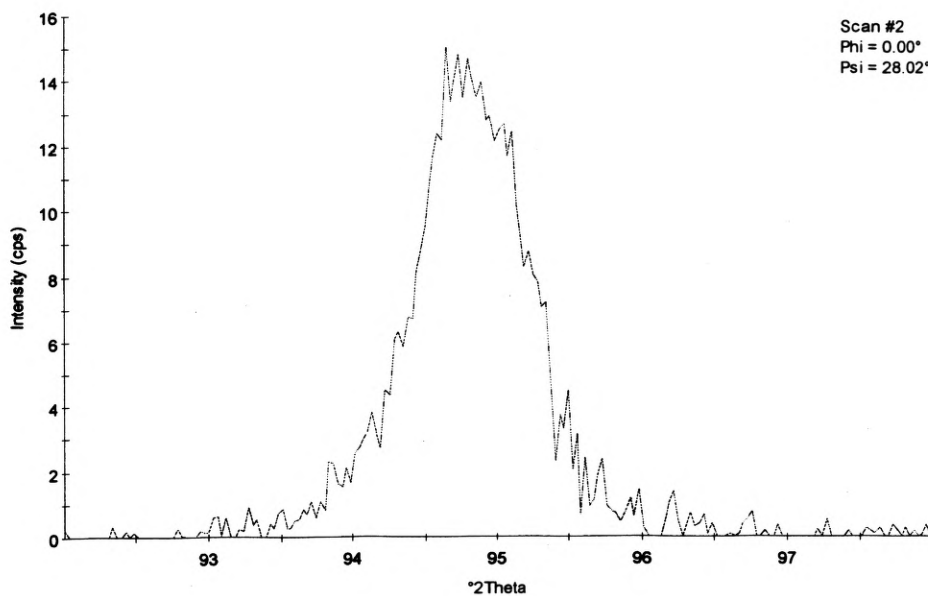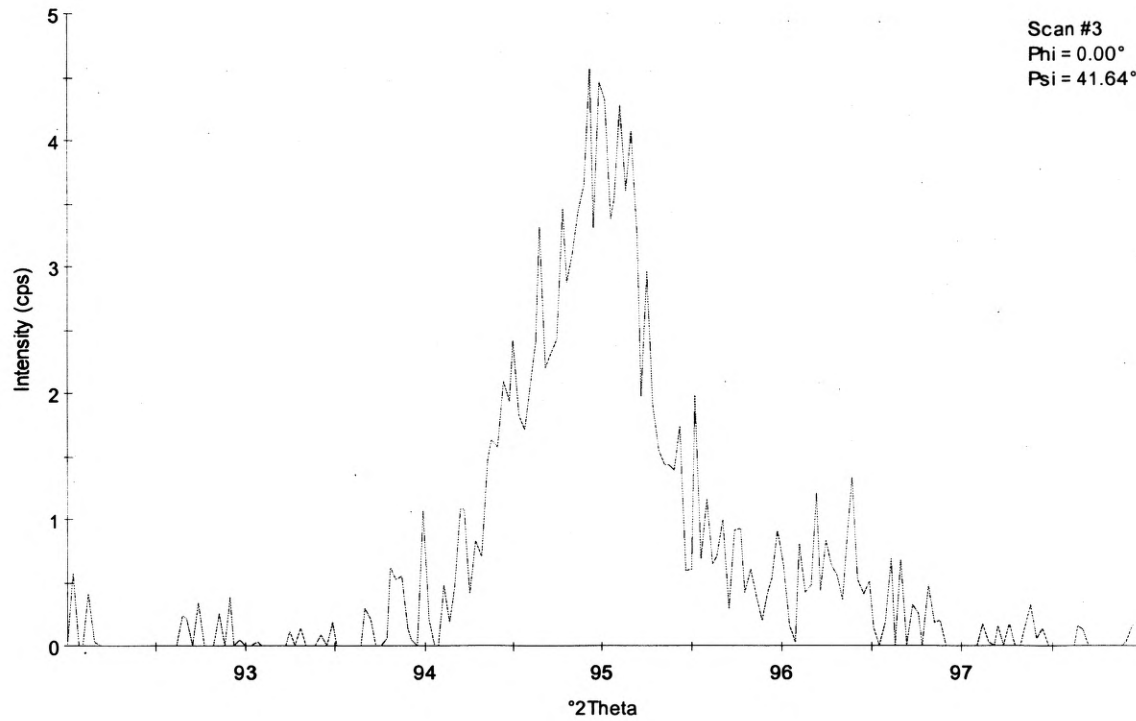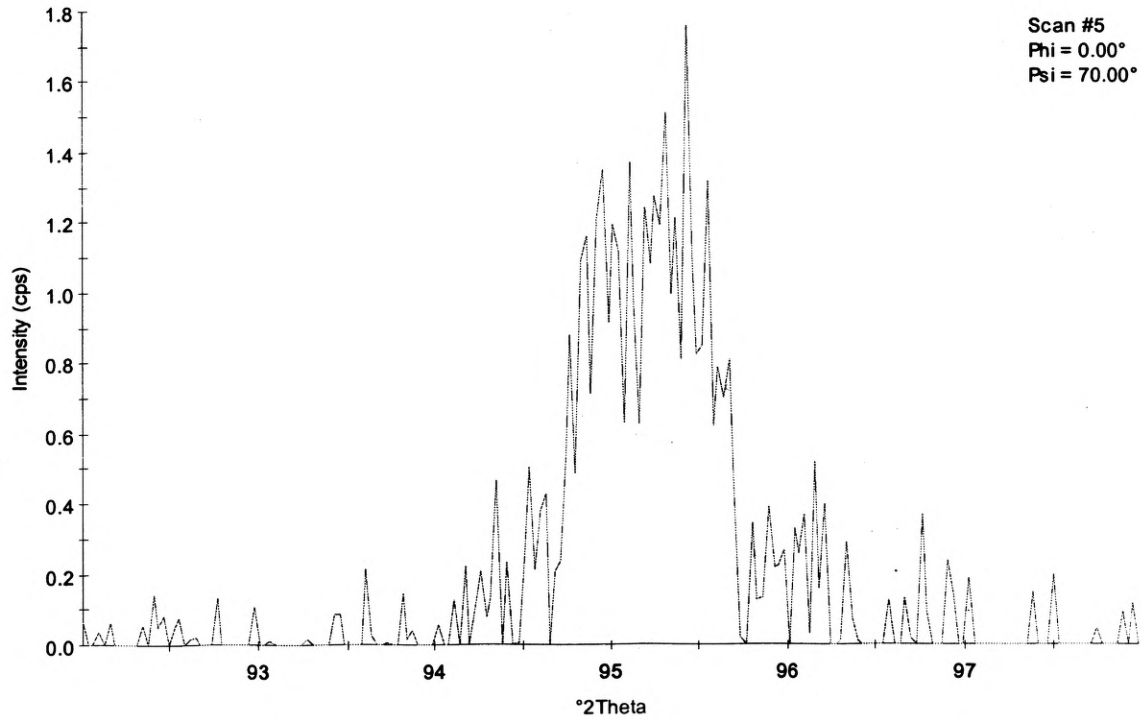Figure 5.39. 2 θ- intensity distribution for ψ =70

As seen in Figure 5.40, the d-spacing is plotted against $\sin^2\psi$ such that the slope of the graph determines the residual stress in the sample. Figure 5.40 shows five points plotted as triangles on the graph. Straight line is fitted using least squares regression for the five points, the slope of which gives the residual stress in the surface of the deposition as described in the residual stress calculation theory earlier(16). The five points are equidistant over a range of 0 to 1 for $\sin^2\psi$ for five different values of ψ, chosen such as to give five equidistant points as seen in Table 5.8. The d-spacing is calculated by the

Bragg's formula for five different values of θ, chosen from the intensity-2 θ distributions shown in Figure 5.35, Figure 5.36, Figure 5.37, Figure 5.38 and Figure 5.39.
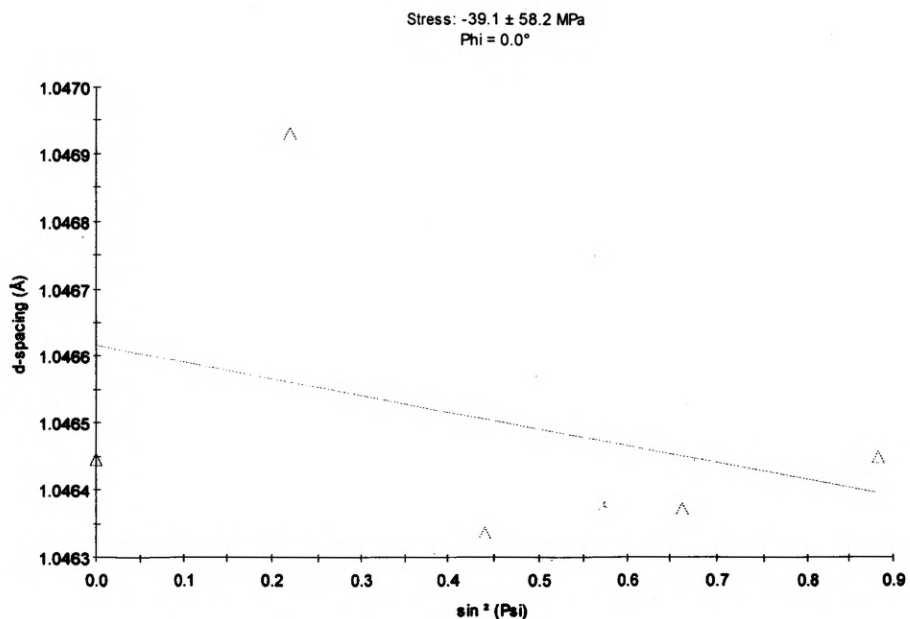
Figure 5.40. Residual stress graph for FGM TBC

Table 5.8. Five peak positions which give highest intensities as seen in the intensity- 2θ graphs and plotted in Figure 5.40

No.	ψ (°)	$\sin^2 \psi$	φ (°)	Peak Pos (°2Theta)	d-spacing (Å)
1	0.00	0	0.00	94.8361	1.04614
2	28.02	0.221	0.00	94.8338	1.04615
3	41.64	0.442	0.00	94.9440	1.04523
4	54.47	0.662	0.00	95.0839	1.04406
5	70.00	0.883	0.00	95.2207	1.04292

5.8. MICROSTRUCTURE ANALYSIS

The cross-section of the deposition was obtained and used to prepare a sample for metallographic analysis. Optical microscope images of the samples were obtained The microstructure analysis of the samples shows the interface between the zirconia, NiCoCrAlY and the substrate. Cracks and pores could be seen at the NiCoCrAlY and zirconia interface that also shows mechanical interlocking in Figure 5.41. This is due to the large difference in the CTE of zirconia and NiCoCrAlY layer. The bulk density of zirconia is 0.65 kg/dm^3 and that of NiCoCrAlY is 3.5kg/dm^3.

As seen in Figure 5.41, the interface between zirconia and NiCoCrAlY has good metallurgical bond.
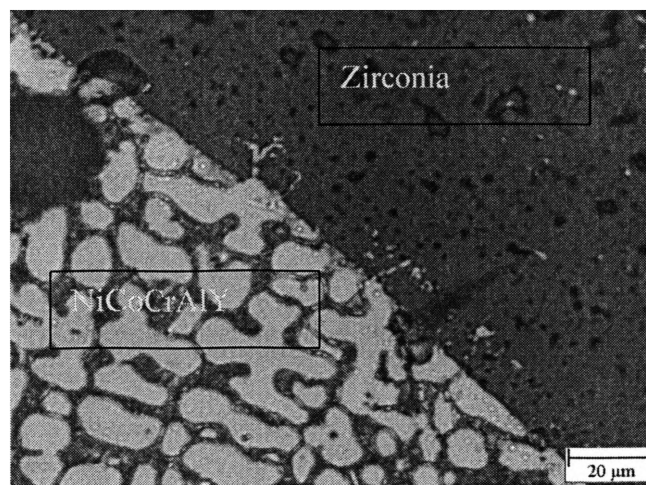
Figure 5.41. Interface between the zirconia and the NiCoCrAlY layer

As seen in Figure 5.42, the NiCoCrAlY layer shows variation in the grain size and orientation. It could be seen that as the depth of the deposition increases the grain size increases. The layers at the top are subjected to rapid heating and cooling cycles giving small grain sizes while the layers at the bottom remain at high temperature for a longer

time causing increased grain sizes. It shows pore and crack free metallurgical bonding at the interface between the NiCoCrAlY and the substrate in Figure 5.43.

Figure 5.42. Grain structure of the NiCoCrAlY layer

Figure 5.43. Interface between the substrate and the NiCoCrAlY layer

5.9. MICROHARDNESS TESTING

Static hardness is defined as the mean contact pressure during indentation, i.e. the applied load divided by the contact area. Traditionally, the residual projected contact area of the imprint is used, which gives the Meyer hardness. With advanced depth-sensing techniques, there is today also possible to determine the contact area continuously during loading, by r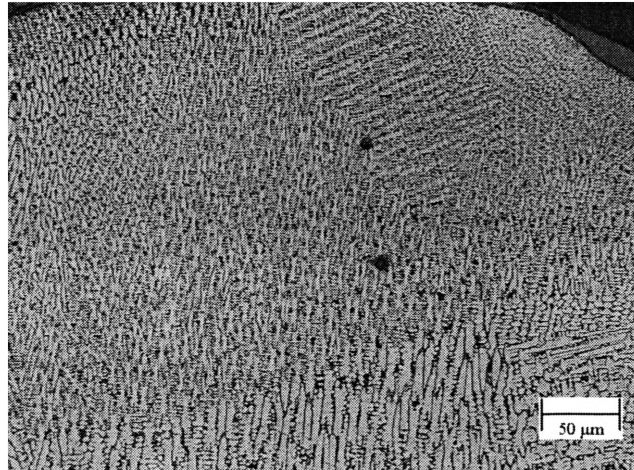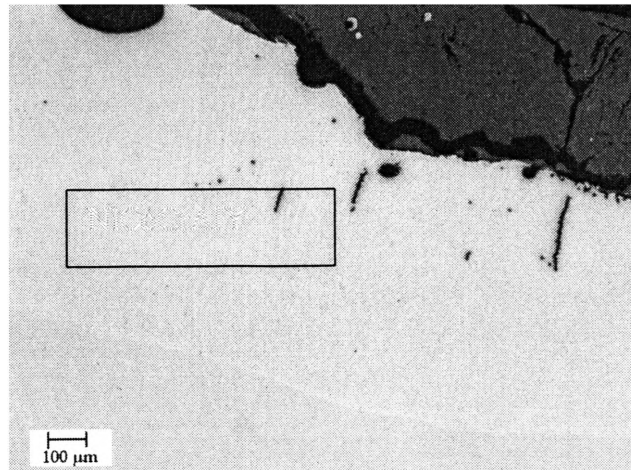elating the geometry of the indenter to the indentation depth. This is a much more efficient way to measure the hardness when performing many and small indents.

The most common types of indenters are the spherical (Brinell), which is blunt and the pyramidal types (Vickers, Cone, Knoop and Berkovitch) which are sharp. The sharp methods develop large plastic deformation directly upon loading through cutting of the indented material, while the spherical type compresses the material, which gives an elastic-plastic deformation. Therefore the sharp methods are more suitable for hardness measurement of hard and brittle material, while the spherical type is restricted to more ductile materials. Further, the hardness of the indenter must always be three times larger than the hardness of the indented material. In sharp indentation diamond is often used as tip material, but spheres of diamond are nearly impossible to produce.

Vickers microhardness test was used to determine the microhardness. As seen in Figure 5.44 and Figure 5.45, total 12 indentations were made out of which 2 were in the epoxy, 1 in the zirconia layer, 4 in the FGM layer and 5 in the substrate. The readings were taken for 10 indentations and the epoxy indentations were not taken into account.

The Vickers microhardness test was done using a load of 0.5 kgf. The Vickers microhardness is shown as HV/0.5, where 0.5 signifies the load used in the testing in kgf. The readings were taken each at an increment of 0.3 mm. The first reading was taken in the zirconia region at 0.12 mm below the surface while the next four readings were taken in the FGM region. The thickness of the zirconia region was 0.34 mm while that of the FGM region was found to be 1.12 mm. Readings at same depths showed similar HV values which also showed similar grain size and direction.
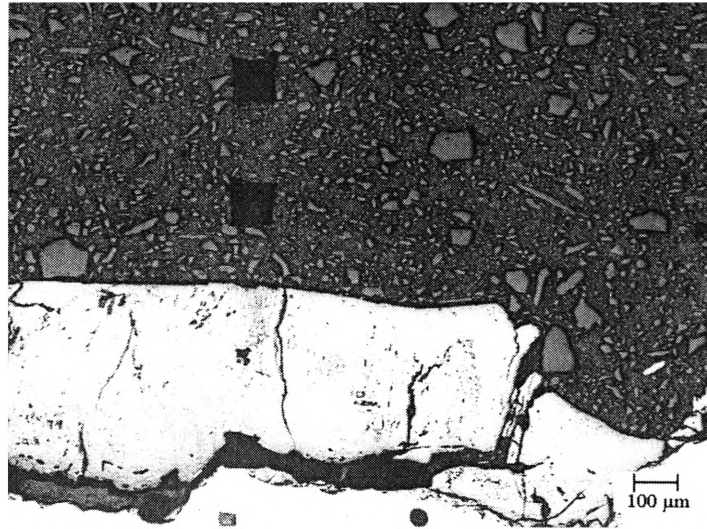
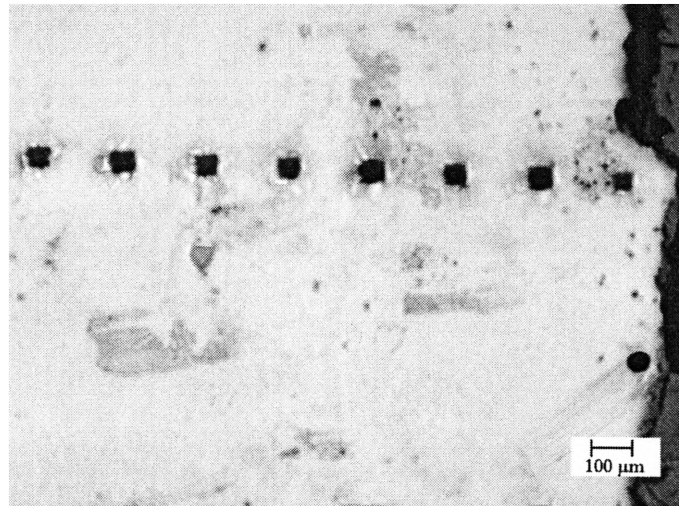Figure 5.44. Vickers microhardness testing indentations

Figure 5.45. Vickers microhardness testing indentations

The microhardness varies from the zirconia layer to the substrate. The zirconia layer gives a microhardness value of 1003HV/0.5. The first reading in the FGM region gives a microhardness of 591.19HV/0.5 and the second reading gives a value of

370.9HV/0.5. There is a sharp change in the microhardness as the depth increases and the zirconia content decreases and the NiCoCrAlY percentage increases causing a decrease in the microhardness. The substrate gives microhardness values of 285.4HV/0.5,300.1HV/0.5, 257.6HV/0.5, 189.2HV/0.5, 183.4HV/0.5. The interface of the zirconia-NiCoCrAlY FGM layer and substrate shows higher values of microhardness because of the mixing of NiCoCrAlY in the substrate during the meltpool formation.

The Vickers microhardness was obtained by calculating the average of the diagonal lengths of each indentation and using the formula

$$HV = (1.8544P)/d^2 \tag{19}$$

Where, P = load in kgf and

d = arithmetic mean of the diagonals of the indentation in mm.

As seen in Figure 5.46, the HV values obtained from the microhardness table, corresponding to the 0.5 kgf are plotted. Table 5.9 gives the average values of the diagonals of each indentation in mm.

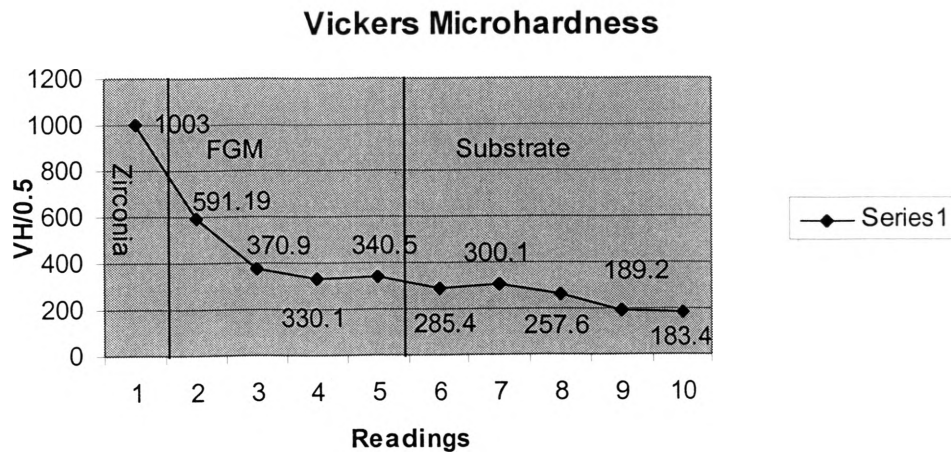Figure 5.46. Microhardness variation along the cross-section of the zirconia and NiCoCrAlY FGM

Table 5.9. Microhardness values along the depth of the coating

No.	d(mm)	HV/0.5
1	0.030	1030
2	0.039	591.19
3	0.050	370.9
4	0.053	330.1
5	0.052	340.5
6	0.057	285.4
7	0.055	300.1
8	0.06	257.6
9	0.07	189.2
10	0.071	183.4

6. DISCUSSION

6.1. EFFECT OF LAMP PARAMETERS ON THE FGM TBC

The effects of each control factor on the deposition characteristic have been discussed in this section.

6.1.1. Power. The influence of power varies as the relative percentages of NiCoCrAlY and Zirconia vary. At 100% NiCoCrAlY, increasing the power decreases the surface quality. As NiCoCrAlY is a low melting point material, increasing the power causes over melting of the deposition and decreases the deposition quality. With higher percentages of zirconia, it being a higher melting point material, increasing the power increases the surface quality measured in terms of surface roughness.

6.1.2. Powder Flow Rate. The influence of powder flow rate is similar with varying composition of NiCoCrAlY and Zirconia. With increasing powder flow rate the quality of deposition decreases. This is because as the powder flow increases the amount of powder that has to be melted by the energy input increases. Also increasing the powder in the deposition increases the possibility of entrapped gases and porosity in the deposition.

6.1.3. Inner Gas. The effect of inner gas becomes more and more prominent with increasing percentage of zirconia. Overall increasing the inner gas pressure increases the surface quality. This could be explained by the fact that increasing the inner gas pressure protects the protective lens during the melting and solidification and reducing oxidation. The main factor is thought to be the effect of inner gas pressure on the mass input to the melt pool. Increase in the inner gas pressure causes most of the powder particles to bounce off causing reduced powder input to the melt pool.

6.1.4. Outer Gas. The effect of outer gas is similar to that of the inner gas. Increasing the inner gas causes a controlled atmosphere and reduces the oxidation. Thus increasing the outer gas pressure increases the surface quality of the deposition. This is because the amount of powder required to be melted is reduced as less powder goes in the melt pool.

6.1.5. Standoff Distance. The standoff distance has an effect on the powder input to the melt pool. The focal point of the powder flow from the nozzle is around 0.35 inches. Thus increasing the standoff distance has an effect similar to that of increasing the powder flow rate. Increasing the standoff distance from 0.25" to 0.35" increases the powder flow rate thus reducing the quality of deposition.

6.1.6. Feed rate. The effect of feed rate on the quality of deposition is a complex phenomenon. Increasing the federate decreases the energy input and at the same time also decreases the mass input of the powder. At lower percentages of zirconia the effect of energy input seems to dominate causing a decrease in the deposition quality with an increase in the feed rate. At higher zirconia percentages the effect of mass input dominates and the deposition quality increases with an increase in the feed rate.

6.1.7. Overlap Increase in overlap causes an increase in the deposition quality.

6.2. EFFECT OF ENERGY INTENSITY ON THE VARIATION OF DEPOSITION QUALITY

The effect of energy intensity on the deposition quality has been analyzed in this discussion.

6.2.1. Energy Intensity. The energy intensity is the amount of energy going into the meltpool at a given instant. There is a threshold of energy intensity below which the material will not melt. If the energy intensity is too low it will lead to incomplete melting and porosity in the depositions. If the energy intensity is too high it will lead to dilution of the depositions, which is the mixing of the depositions with the substrate material leading to poor deposition qualities.

$$E = P/(d*v) \tag{20}$$

E-Energy Intensity in Joules.

P- Power in Watts.

d-Laser spot diameter in meters.

V-Feedrate in m/s.

As seen in Figure 6.1, the variation of surface roughness of 100% NiCoCrAlY and 0% zirconia for the variation in energy density is shown.
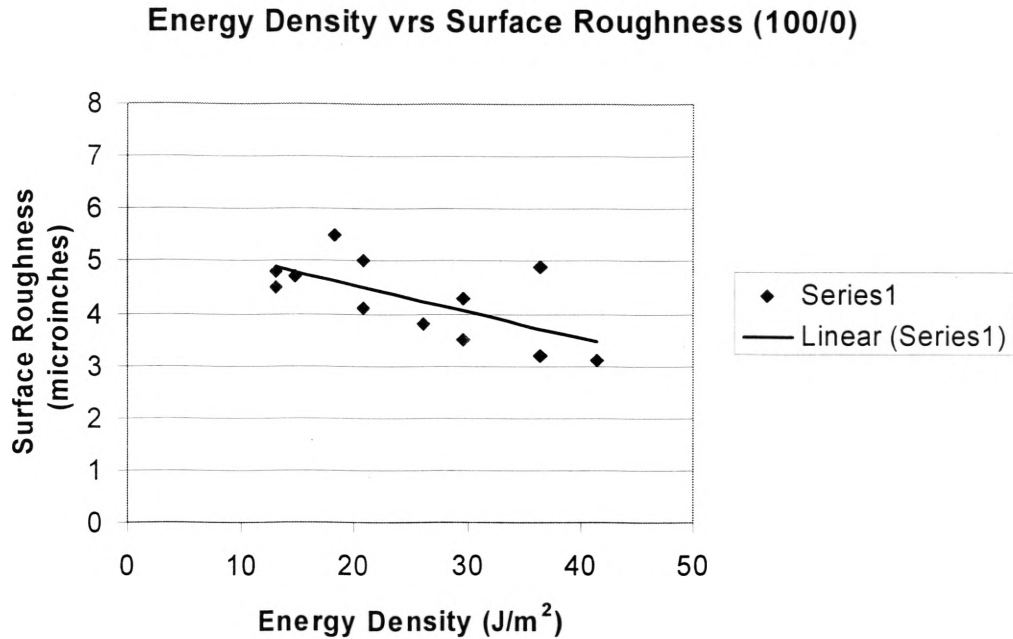
Energy Density vrs Surface Roughness (100/0)

Figure 6.1. Energy density vs. surface roughness for 100% NiCoCrAlY and 0% zirconia

As seen in Figure 6.2, the variation of surface roughness of 80% NiCoCrAlY and 20% zirconia for the variation in energy density is shown. The X axis represents the energy density while the Y axis represents the surface roughness in micro inches.

As seen in Figure 6.3, the variation of surface roughness of 60% NiCoCrAlY and 40% zirconia for the variation in energy density is shown. The X axis represents the energy density while the Y axis represents the surface roughness in micro inches.

As seen in Figure 6.4, the variation of surface roughness of 40% NiCoCrAlY and 60% zirconia for the variation in energy density is shown. The X axis represents the energy density while the Y axis represents the surface roughness in micro inches.

As seen in Figure 6.5, the variation of surface roughness of 20% NiCoCrAlY and 80% zirconia for the variation in energy density is shown. The X axis represents the energy density while the Y axis represents the surface roughness in micro inches.

Figure 6.2. Energy density vs. surface roughness for 80% NiCoCrAlY and 20% zirconia

Figure 6.3. Energy density vs. surface roughness for 60% NiCoCrAlY and 40% zirconia

Energy Density vrs Surface Roughness (40/60)

Figure 6.4. Energy density vs. surface roughness for 40% NiCoCrAlY and 60% zirconia

As seen in Figure 6.6, the variation of surface roughness of 0% NiCoCrAlY and 100% zirconia for the variation in energy density is shown. The X axis represents the energy density while the Y axis represents the surface roughness in micro inches.

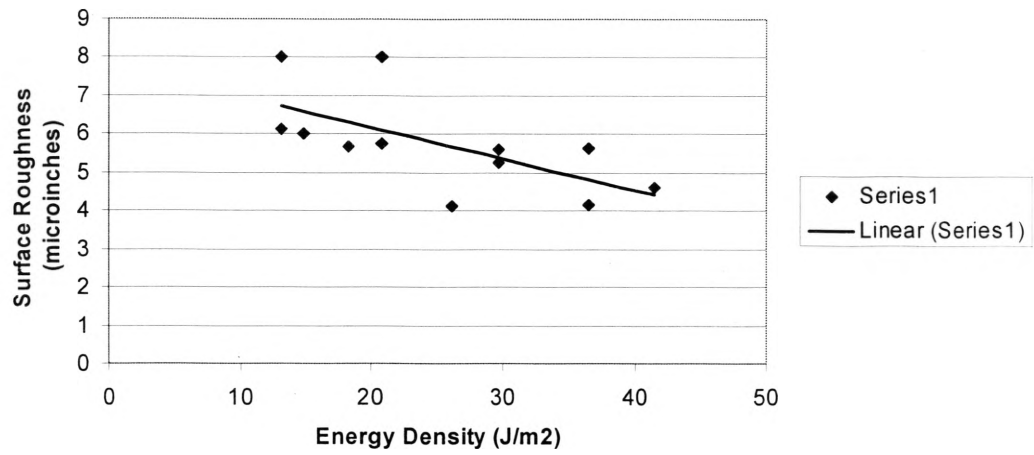Energy Density vrs Surface Roughness (20/80)

Figure 6.5. Energy density vs. surface roughness for 20% NiCoCrAlY and 80% zirconia
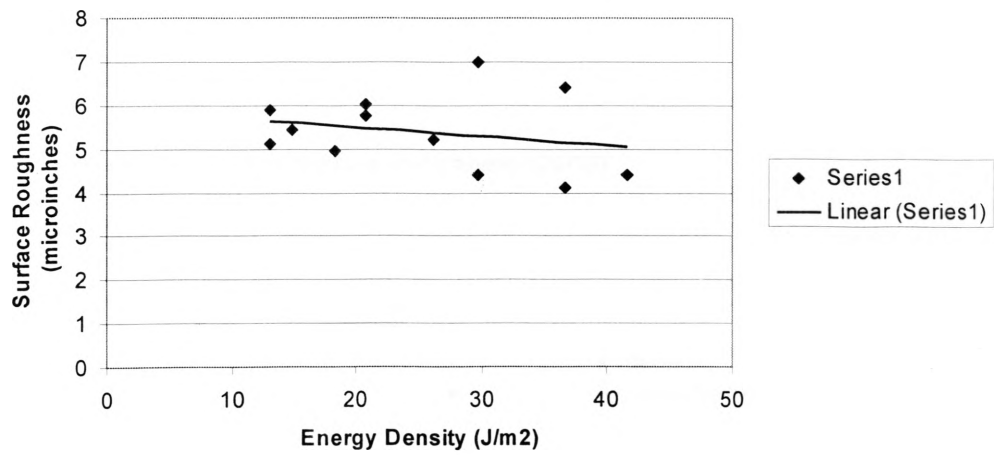
Energy Density vrs. Surface Roughness(0/100)

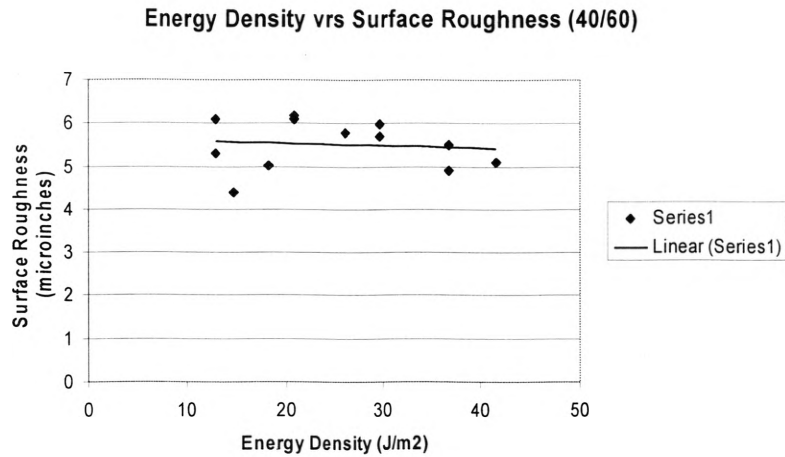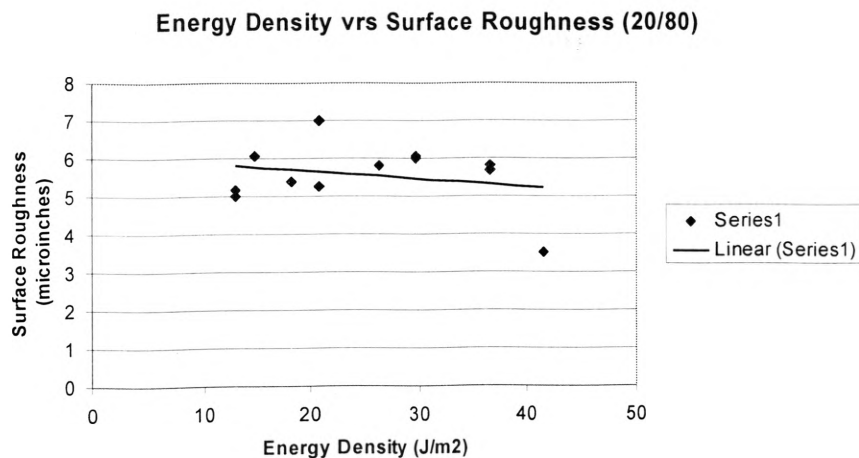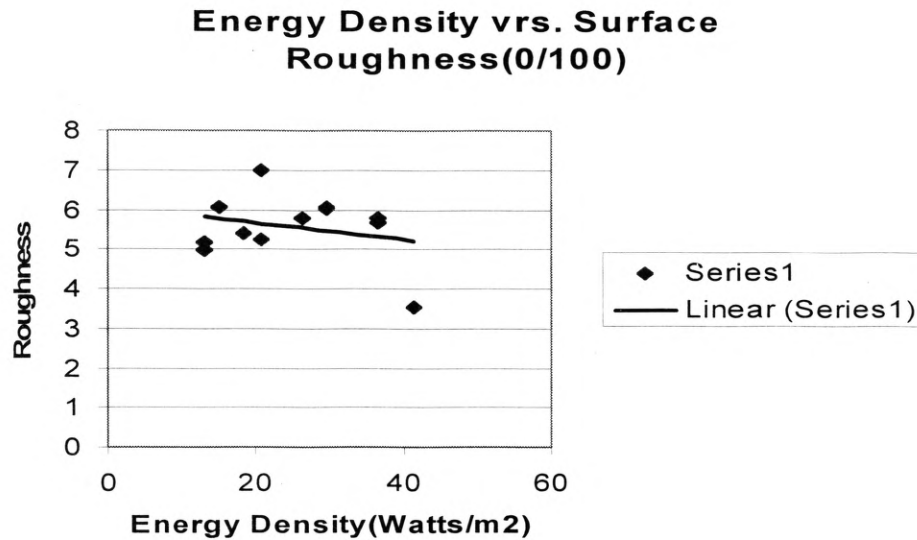Figure 6.6. Energy density vs. surface roughness for 0% NiCoCrAlY and 100% zirconia

6.2.2. Effect of Zirconia Variation on the Deposition Quality with the Variation in Energy Density. It was observed that as the zirconia content in the FGM increases and the NiCoCrAlY content decreases the energy intensity required to melt the material increases. This can be observed that with the increase in the zirconia content the surface roughness increases and the average surface roughness curve shifts to the upper right side on a plot of energy intensity vrs surface roughness for increasing zirconia content in the FGM. This is because the melting point of zirconia is 2700 F which is very high as compared to NiCoCrAlY. For the same settings with different material compositions the energy intensity required to melt the powders increases. This causes increase in the average surface roughness value for increasing zirconia content in the deposition. Interesting observation was that at maximum energy intensity the surface roughness was the least for all the depositions.

The energy intensity has a lower threshold below which the energy input into the melt pool will not be sufficient to melt the powder. This leads to increased porosity and increased surface roughness causing bad deposition. Increased energy intensity causes extra energy input to the melt pool causing dilution of the deposits.

Energy intensity alone does not ensure reduced porosity and good depositions. Other factors such as inner gas, outer gas and standoff distance determine the amount of powder going in the melt pool. Increasing the gas pressure causes more powder to bounce off the substrate and the amount of powder being deposited reduces. This depends on the density, particle size, shape of the powder. Standoff distance equal to the focal length of the nozzle causes maximum powder to enter the melt pool. Varying the standoff distance on either side causes a reduction in the powder entering the melt pool. As seen in Figure 6.7, the variation of surface roughness for zirconia content and variation in energy density is shown.
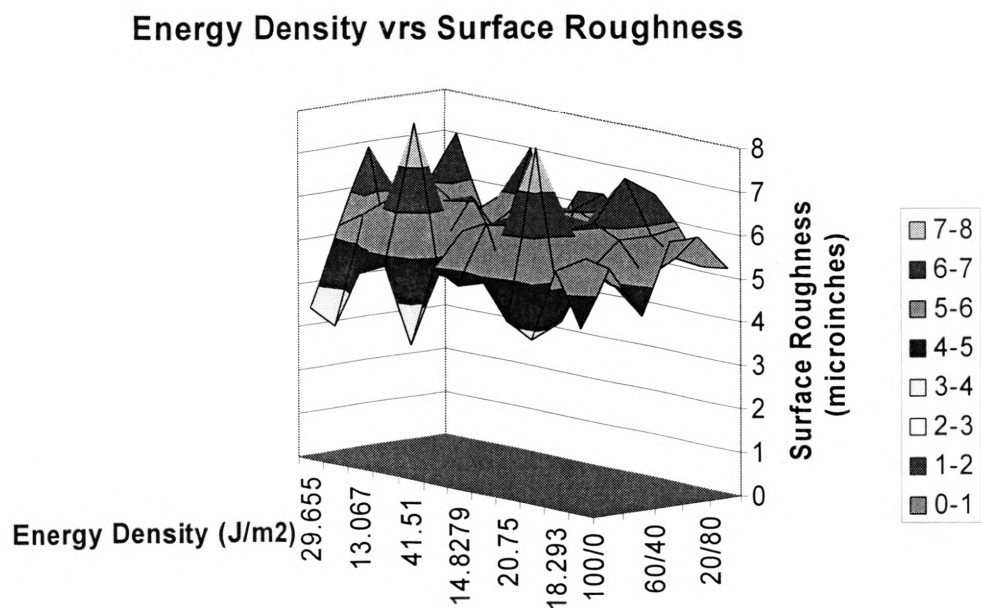
Figure 6.7. Variation of surface roughness with energy density for different compositions of the coating

6.3. RESIDUAL STRESS

The wide operating temperature range of the TBC causes differential expansion and contractions of the substrate, bond coat and the ceramic layer inducing tensile stresses in the ceramic layer, since it has lower CTE than the bond coat. This cyclical variations in the stresses cause initiation and widening of cracks leading to failure of the coatings.

The LAMP TBC deposition has a resultant compressive residual stress of 39.1 MPa, which is beneficial for improved life of the coatings. The values reported in the literature for conventional as-deposited coatings are 70 MPa and 3.5 GPa for as sprayed TBC and thermally grown oxide (TGO) layers.

7. CONCLUSION

Optimization of LAMP parameters for low surface roughness of FGM depositions for NiCoCrAlY and zirconia was done over a range of parameters. Surface roughness was chosen as the defining criterion because it can be considered as a reflection of deposition quality as explained earlier. The percentage influence of each factor and its variation with changing zirconia percentage is obtained by the Analysis of Variance (ANOVA). The values of parameters thus obtained were used to deposit samples which were subjected to residual stress, microstructure and microhardness analysis. The variation of surface roughness with the energy density and zirconia percentage is plotted to get their effect on the surface roughness. A study of the effect of energy density changes on the surface roughness of the coatings for varying compositions of the deposits in a functionally graded coating was carried out. Taguchi approach of Design of Experiments was used to optimize the process conditions and the relative influence of each process parameter was obtained. The variation of the influence of each parameter with varying composition of the functionally graded coating is analyzed to draw inferences on the trend of variations.

Power- As NiCoCrAlY is a low melting point material, increasing the power causes overmelting of the deposition and decreases the deposition quality. With higher percentages of zirconia, it being a higher melting point material, increasing the power increases the surface quality measured in terms of surface roughness.

Powder flow rate- With increasing powder flow rate the quality of deposition decreases.

Inner Gas Pressure- Overall increasing the inner gas pressure increases the surface quality.

Outer Gas Pressure- Increasing the outer gas pressure increases the quality of deposition.

Standoff distance- Increasing the standoff distance from 0.25" to 0.35" increases the powder flow rate thus reducing the quality of deposition.

Feedrate- Increasing the federate decreases the energy input and at the same time also decreases the mass input of the powder. At lower percentages of zirconia the effect

of energy input seems to dominate causing a decrease in the deposition quality with an increase in the feed rate. At higher zirconia percentages the effect of mass input dominates and the deposition quality increases with an increase in the feed rate.

Overlap- Increase in overlap causes an increase in the deposition quality. The samples showed pore free interface between the substrate and the NiCoCrAlY but cracks and porosity in the zirconia layer. The microhardness testing shows gradient in the microhardness of the coating along the depth. Further studies on the comparison with the conventional established processes of TBC deposition need to be done for establishing this process for TBC deposition.

Residual stress analysis results of the coating samples obtained by using optimized parameters of deposition show a small amount of compressive stress of 39MPa in the deposited coatings. This can be compared with the literature values of residual stress in the TBC and Thermally Grown Oxide (TGO) layers of 70MPa and 3.5GPa. This makes LAMP a potential candidate for TBC deposition. The comparison between the LAMP deposits and the TBC coatings obtained by conventional processes is the next step to compare and establish the viability of the LAMP for the TBC deposition. The study indicates the LAMP deposition samples show crack and pore free interface between the NiCoCrAlY layer and the substrate with fine columnar microstructure in the NiCoCrAlY layer with low surface roughness. LAMP could be used to deposit the NiCoCrAlY bondcoat after further tests need to confirm that.

BIBLIOGRAPHY

1. L. Singheiser, R. Steinbrech, W. J. Quadakkers and R. Herzog. "Failure Aspects of Thermal Barrier Coatings," Science Reviews, Materials at High Temperatures, 18(4), 2001, 249-259.

2. S. Takahashi, M. Yoshiba and Y. Harada. "Microstructural Features of Mechanical Failure in thermal barrier coating systems under static loadings," Science Reviews, Materials at High Temperatures, 18(2), 2001, 125-130.

3. R. Viswanathan, S. T. Scheirer. "Materials Technology for Advanced Land Based Gas Turbines," No. 1-201, Proceedings of CREEP, JSME, 2001.

4. H. Bernstein, J. Russell, S. Scheirer, L.L. Hsu and M.van Roode. Guidebook and Software for Specifying High Temperature Coatings for Combustion Turbines. EPRI, 1983.

5. J. Wesley Cox. Wear and Corrosion Resistant Hard Coatings for Non Cutting Tool Applications. William Andrew Publishing, 2001.

6. I. G. Wright and B. A. Pint. "Materials Research in Support of Industrial Gas Turbines," Intl. Conference on Industrial Gas Turbine Technology (CAME-GT), 2003.

7. I. Kvernes, E. Lugscheider and F. Ladru. "Lifetime and Degradation Processes of TBCs for Diesel Engines," Proceedings of 6th Liege Conference on Materials for Advanced Power Engineering, 1998, 997-1012.

8. K. Yasuda, S. Suenaga, H. Inagaki, Y. Goto, H. Takeda and K. Wada. "Relationship between microstructure of plasma-sprayed 8YZ coatings and thermal fatigue life of thermal barrier coatings," Journal of Materials Science, 35(2), 2000, 317-321.

9. K. A. Khor. "Properties of Plasma Sprayed Functionally Graded YSZ/NiCoCrAlY Composite coatings," Journal of Surface and Coatings Technology, Volume:139, Issue: 2-3, 2001, 200-206.

10. T. Elperin and G. Rudin. "Thermal Reliability Testing of Functionally Graded Coatings Using Laser Thermal Shock Method," Israel- Japan Workshop, Dynamic Response of Brittle Solids, 2001.

11. S. Ahmaniemi "Characterization of Modified Thick Thermal Barrier Coatings," Thermal Spray 2003:Advancing the Science and Applying the Technology,Published by ASM International, 2003, 1477-1486.

12. M. Eskner. "Mechanical Behavior of Thermal Barrier Coatings," Dissertation Royal Institute of Technology Sweden, 2004.

13. M. Gell, Eric Jordan, Krishnakumar Vaidyanathan, Kathleen McCarron, Brent Barber, Yong-Ho Sohn and Vladamir K.Tolpygo. "Bond strength, bond stress and spallation mechanisms of thermal barrier Coatings," Vol 120-121, 1999, 53-60.

14. R. K. Roy. Design of Experiments Using the Taguchi Approach. Wiley- Interscience, 2001.

15. M. J. Stiger, L.A. Ortman, F.S. Pettit and G.H. Meier. "Measurement of Interfacial Toughness in Thermal Barrier Coating Systems by Indentation," Presented at Wright-Patterson Airforce Base, 1999.

16. P. S. Prevey. "X-ray Diffraction Residual Stress Techniques." www.lambda-research.com

VITA

Yashodhan Vinay Joshi was born on June 30, 1979 at Aurangabad, India. He graduated from Saraswati Bhavan Highschool Aurangabad and later received his B.S. degree in Mechanical Engineering from Marathwada University, Aurangabad, in May 2000. He worked as a Co-op with La-Z-Boy, Arkansas as a Process Improvement Engineer from June 2004 to October 2004. In May 2005, he received his M.S. degree in Manufacturing Engineering from the University of Missouri-Rolla, Rolla, Missouri, USA. He will be working with Trey Young Metal Works, Missouri, as a Production Manager.

He has authored two papers while working for his Masters at University of Missouri-Rolla in Manufacturing Engineering. 'Application of Laser Aided Manufacturing Process for Part Repair: A Review' was presented in the SFF symposium 2002 at Austin, Texas while 'Application of Laser Aided Manufacturing Process for Functionally Graded Thermal Barrier Coatings' has been accepted for ICALEO conference 2004 at San Francisco, California.